Compressibility effects on the structural evolution of transitional high-speed planar wakes

Jean-Pierre Hickey[1],†, Fazle Hussain[2] and Xiaohua Wu[1]

[1]Department of Mechanical and Aerospace Engineering, Royal Military College of Canada, Kingston, Ontario K7K 7B4, Canada

[2]Department of Mechanical Engineering, Texas Tech University, Lubbock, TX 79409, USA

The compressibility effects on the structural evolution of the transitional high-speed planar wake are studied. The relative Mach number (Ma_r) of the laminar base flow modifies two fundamental features of planar wake transition: (i) the characteristic length scale defined by the most unstable linear mode; and (ii) the domain of influence of the structures within the staggered two-dimensional vortex array. Linear stability results reveal a reduced growth (approximately 30 % reduction up to $Ma_r = 2.0$) and a quasilinear increase of the wavelength of the most unstable, two-dimensional instability mode (approximately 20 % longer over the same Ma_r range) with increasing Ma. The primary wavelength defines the length scale imposed on the emerging transitional structures; naturally, a longer wavelength results in rollers with a greater streamwise separation and hence also larger circulation. A reduction of the growth rate and an increase of the principal wavelength results in a greater ellipticity of the emerging rollers. Compressibility effects also modify the domain of influence of the transitional structures through an increased cross-wake and inhibited streamwise communication as characteristic paths between rollers are deflected due to local Ma gradients. The reduced streamwise domain of influence impedes roller pairing and, for a sufficiently large relative Ma, pairing is completely suppressed. Thus, we observe an increased two-dimensionality with increasing Mach number: directly contrasting the increasing three-dimensional effects in high-speed mixing layers. Temporally evolving direct numerical simulations conducted at $Ma = 0.8$ and 2.0, for Reynolds numbers up to 3000, support the physical insight gained from linear stability and vortex dynamics studies.

Key words: compressible turbulence, transition to turbulence, wakes

1. Introduction

Understanding high-speed transitional wakes is of great interest in scramjet engines, aero-optic laser diffraction and transonic turbomachinery. At the heart of this interest

† Present address: Department of Mechanical and Mechatronics Engineering, University of Waterloo, Waterloo, Ontario N2L 3G1, Canada. Email address for correspondence: jean-pierre.hickey@uwaterloo.ca

lies the desire to modify, predict and/or control the large-scale coherent structures originating during transition. This is especially important as wakes interact with other canonical flows in most applications (Wu *et al.* 1999; Wu & Hickey 2012). From an engineering perspective, these highly anisotropic transitional structures are important for their mixing enhancement potential as they are the main contributors to the large-scale entrainment (Brown & Roshko 1974), a generally desired attribute for fuel injector systems. At the same time, these structures are one of the primary sources of aeroacoustic disturbances resulting from the large pressure gradients and vortical reconnection (Sandham 1994; Virk, Hussain & Kerr 1995; Bastin, Lafon & Candel 1997; Hussain & Duraisamy 2011) which, downstream, may lead to combustion oscillations in supersonic propulsion systems (Choi, Ma & Yang 2005). In order to control these conflicting characteristics, the effects of compressibility on the transitional high-speed wake need to be much better understood.

Characterizing compressibility effects. Insight into compressibility effects (understood herein as Mach number effects) in free-shear flows has historically been gained through the study of the high-speed mixing layer – a simple and ubiquitous free shear flow. The most intriguing effect is the reduced lateral spreading with increased convective Mach number, Ma_c. From early experiments, the reduced turbulent kinetic energy (TKE) could qualitatively explain the lower spread rate; density variations only have a second-order effect (Brown & Roshko 1974). What is less clear is the exact mechanism by which compressibility limits TKE growth. From the governing equations, the evolution of TKE for a compressible flow is written as

$$\frac{\mathrm{d}K}{\mathrm{d}t} = P + \Sigma^d - \overline{\epsilon}_s - \overline{\epsilon}_d, \tag{1.1}$$

where P, Σ^d, $\overline{\epsilon}_s$ and $\overline{\epsilon}_d$ are respectively the production, pressure-dilatation correlation, solenoidal dissipation and dilatational dissipation. Early works attributed the lower turbulent kinetic energy to a negative pressure–dilatational and dilatational dissipation terms in shear flows (Zeman 1990; Sarkar, Erlebacher & Hussaini 1991). But the dilatation alone cannot account for the extent of the TKE reduction as the increased dilatation with Ma is modest apart from a very limited region of the flow found within a shock wave. Breidenthal (1992) proposed a novel structural explanation for the reduced spread rate using a sonic-eddy model to account for the reduced entrainment of high-speed flows. Numerical simulations have led us to conclude that the reduction of the pressure–strain term implicitly inhibits the turbulence production by reducing the transfer among velocity components (Blaisdell, Mansour & Reynolds 1993; Vreman, Sandham & Luo 1996; Pantano & Sarkar 2002; Foysi & Sarkar 2010). Naturally, the delayed return to isotropy caused by the finite propagation speed of the acoustic waves modifies the near-field anisotropy of the flow (Pantano & Sarkar 2002). Pantano & Sarkar (2002) showed, using an analysis based on the wave equation of a pressure perturbation, that the pressure–strain term decreases monotonically with increasing Ma as the acoustic interaction time increases.

Fewer studies have specifically tackled compressibility effects in the planar wake. This is partly because the compressibility effects, characterized by the relative Mach number $Ma_r = U_o/c_\infty$ (where U_o is the centreline velocity defect and c_∞ the free-stream speed of sound), are not constant and, therefore, more difficult to isolate than in the mixing layer. As Ma_r monotonically decreases with the wake evolution, so does the influence of compressibility. The coupling between the compressibility and the wake evolution raises an important question on the scaling of the wake. On one

hand, if compressibility inhibits the spread rate through reduction of the pressure–strain term, as is the case for the mixing layer, the wake half-width appears to be an ill-suited non-dimensionalization parameter, as the spread rate would reduce with reducing compressibility as the wake evolves. On the other hand, if the spread rate remains invariant to the decreasing Ma_r with the wake evolution (in the mid- and far-wake when compressibility may still be non-negligible), a structure-based explanation must be sought for the contrast with the mixing layer results. Even though the wake tends toward a fully incompressible state as the velocity defect becomes null, it does not necessarily mean that the self-similar states of the incompressible and high-speed wakes are identical. Since free-shear flows maintain a 'memory' of their origin, it can be inferred that a differing far-wake structural organization and statistics found by Bonnet *et al.* (1991) and Hickey, Hussain & Wu (2013) may be related to the near-wake and/or transitional evolution.

Transition of planar wakes. As for all shear flows, the compressibility has a stabilizing effect in the wake (Behrens 1968; Demetriades 1971), a finding confirmed by hydrodynamic stability calculations (Chen, Cantwell & Mansour 1990; Watanabe & Maekawa 2004). In contrast to the obliquity of the primary instability mode in the high-speed mixing layer (above $Ma_c = 0.6$), a two-dimensional anti-symmetric mode is found to be dominant for all Mach numbers in the planar wake (Chen *et al.* 1990). This result was nuanced by Papageorgiou (1990) who questioned the validity of the parallel flow assumption inherent in the temporal stability calculations and showed that a three-dimensional wave inclined at 60° has the highest growth rate for spatially evolving wakes with a Gaussian velocity profile at $Ma_\infty = 3.0$. The obliquity of the transitional mode was experimentally observed by Lysenko (1999) by artificially forcing a splitter-plate wake at $Ma_\infty = 2.0$. It is unclear why the observed oblique perturbation undergoes the largest growth. It could be related to one of the following reasons: (i) the growth of the most unstable oblique mode, as found by Papageorgiou (1990); (ii) as hypothesized by Lysenko (1999), a receptivity of an inclined symmetric mode which emerges for $Ma_r > 1.2$ (Watanabe & Maekawa 2004); (iii) a secondary acoustic mode which resonates between the sonic lines of the wake as in the boundary layer (Mack 1990); or (iv) a triadic nonlinear interaction as observed in the *H*-type transition in the boundary layer (Hebert 1988). The debate surrounding the origin of the three-dimensional modes remains open and central to the understanding of the transitional mechanism of the planar wake.

Structures in high-speed flows. There has been some debate on the presence (or absence) of transitional spanwise coherent rollers in the planar wake. Kendall (cited in Laufer (1975)) noted a clear absence of structures in the transitional region. More recently, experiments by Clemens & Smith (1998) found that the high-speed wake shares many structural similarities with its incompressible counterpart, most importantly in terms of the two-dimensionality of the transitional rollers connected by rib-like structures. From experiments, it is difficult to establish the origin of the transitional structures, as they may emerge due to linear growth of an unstable mode or due to the receptivity of the unsteady Kutta condition (Barone & Lele 2005). Alternatively, the structures may also originate from the two-dimensional convective instability in the base flow (Sandham & Sandberg 2009). What is clear, is that the wake and the transitional structures are highly sensitive to the splitter-plate design (Althaus 1990). In the intermediate and far wake, the two-dimensionality of the structures has been well established (Bonnet & Chaput 1986; Nakagawa & Dahm 2006) having a Strouhal number of 0.3 (Behrens & Ko 1971; Gai, Hughes & Perry 2002).

Direct numerical simulations of idealized wakes help clarify the transitional mechanisms and structures. Using a laminar base flow with eigenmode perturbations, Chen *et al.* (1990) and Watanabe & Maekawa (2004) showed many qualitative similarities with the low-speed wake: two-dimensional and staggered spanwise rollers connected by rib-like structures. This apparent structural invariance to *Ma* contrasts the emergence of Λ-type structures in the high-speed mixing layer (Kourta & Sauvage 2002). When the base flow was perturbed with broadband random fluctuations (Watanabe & Maekawa 2004), an oblique mode briefly dominates the early wake evolution before being overtaken by the growth of the primary two-dimensional mode: clearly an unexpected finding based on linear stability results. Unfortunately, the available direct numerical simulations of high-speed planar wakes (Chen *et al.* 1990; Watanabe & Maekawa 2004) are inadequate to fully understand the origin of the three-dimensional modes. More specifically, it is unclear if they are caused by an oblique principal mode, or by the receptivity of a secondary symmetric mode. The reasons for the inadequacy of existing DNS simulations are: (i) the limited streamwise and spanwise computational domains (L_x twice the most unstable wavelength (Chen *et al.* 1990)) cannot capture the symmetric instability mode which is over twice the streamwise wavelength at $Ma = 2.0$, (ii) the low Reynolds number of the simulations ($Re = 300$ in Chen *et al.* (1990) and up to $Re = 1000$ in Watanabe & Maekawa (2004)) limits the growth of the oblique instability mode, which is shown herein to be very sensitive to viscous effects at low Reynolds numbers. These shortcomings invite a closer investigation of transitional mechanisms with modern day computational resources with a canonical set-up, free of trailing edge effects.

In this work, we seek to elucidate the influence of compressibility on the transitional structures of the planar high-speed wake. We shed light on some lingering questions: what is the effect of compressibility on the structures in the transitional flow? How does the *Ma* influence the structural pairing of rollers? What is the effect on the turbulence anisotropy? What is the influence of compressibility on the three-dimensionality of the wake? The present investigation rests on a combined study using linear stability analysis, vortex dynamics and direct numerical simulations of the transitional high-speed wake to gain insight into the flow physics. The paper is organized as follows. The details of the linear stability analysis and numerical simulations are presented in the § 2. The stability results are detailed in § 3. Based on these findings and an idealized understanding of the wake, we infer the structural features of the nonlinear stage of transition in § 4. These theoretical results are supplemented by direct numerical simulations of the transitional high-speed wakes in which the statistics and structural evolution are respectively presented in §§ 5 and 6.

2. Numerical details

2.1. *Viscous linear stability theory*

A viscous, compressible linear stability analysis tool was developed to study the transitional characteristics of the high-speed planar wake based on the previous work by Chen *et al.* (1990) and Watanabe & Maekawa (2004). A periodic disturbance, with given streamwise and spanwise wavelengths, is applied to a laminar base flow. The temporal growth of the perturbation is computed from the linearized three-dimensional Navier–Stokes equations (conservation of mass and momentum) and the energy equation in non-conservative form. To assure the validity of the linear assumption, we impose a very low-amplitude perturbation to the base flow of the form: $\boldsymbol{\Phi} = \hat{\boldsymbol{\Phi}} \exp(\mathrm{i}(\alpha x + \beta y - \omega t))$, where $\boldsymbol{\Phi}$ represents a vector of the primitive

variables: $[\rho, u, v, w, T]$. For a temporal stability calculation, α and β are real and respectively the streamwise and spanwise wavenumbers, while ω is complex with the imaginary part being the temporal growth rate of the given perturbation. Assuming a parallel flow, we consider the stability characteristics of an initial Gaussian velocity profile: $U(y) = U_\infty - U_0 \exp(-\ln(2)y^2)$, where U_∞ and U_0 are respectively the free-stream velocity and centreline defect. These values are chosen to compare our results with the previous investigations (Chen *et al.* 1990; Watanabe & Maekawa 2004). The thermodynamic quantities are related through the ideal gas equation of state where the non-dimensionalized static pressure was assumed to be constant across the wake. The initial temperature and density profiles were determined using the Crocco–Busseman relation with a unitary Prandtl value. In the cross-wake direction, a hyperbolic tangent stretching was used to convert the doubly infinite domain to a finite computational domain defined on $\zeta = [0, 1]$ using the spectral mapping techniques by Cain, Ferziger & Reynolds (1984). The linearized equation set can be solved as a simple eigenvalue problem of the form $\mathscr{L}\hat{\boldsymbol{\Phi}} = \omega\hat{\boldsymbol{\Phi}}$ where $\mathscr{L}$ is a linear operator acting on the eigenvector $\hat{\boldsymbol{\Phi}} = [\hat{\rho}, \hat{u}, \hat{v}, \hat{w}, \hat{T}]$ for a given eigenvalue, ω. The eigenvalue with the largest imaginary part represents the maximal growth of the imposed perturbations. By investigating the resulting real part of the eigenvectors of the equation, we distinguish between the symmetric (varicose) and anti-symmetric (sinuous) modes. The complete mathematical formulation of the problem can be found in Watanabe & Maekawa (2004) and is not repeated. Numerically, the eigenvalue calculations are performed using the LAPACK scientific library. A gradient-based sequential least-squares programming algorithm (SLSQP), implemented through the pyOpt package (Perez, Jansen & Martins 2012), was used to reduce the computational time required to identify the optimal growth over the solution domain. We confirmed the validity of our linear stability code by comparing our results with previously calculated linear stability statistics from Chen *et al.* (1990) and Watanabe & Maekawa (2004). The linear stability source code can be found in Hickey (2012).

2.2. *Direct numerical simulation details*

2.2.1. *Governing equations*

The solved equation set for direct numerical simulation, written in conservative form, consists of the equations for mass, momentum and total energy along with an additional passive scalar equation. The equations are non-dimensionalized by the free-stream velocity, $U = U_\infty$ and the initial wake half-width, $L = b_0$. The other parameters are non-dimensionalized with the free-stream values. The corresponding non-dimensional pressure and energy are respectively $p = p^* \rho_0 c_0^2 / \gamma$ and $E = E^* / \rho_0 U^2$, while the Reynolds, Prandtl and Mach numbers are

$$Re = \frac{\rho_0 UL}{\mu_0}; \quad Pr = \frac{\mu_0 c_p}{\kappa_0}; \quad Ma = \frac{U}{c_0}. \quad (2.1a\text{--}c)$$

The non-dimensionalized governing equations are

$$\left.\begin{array}{c} \dfrac{\partial \rho}{\partial t} + \dfrac{\partial(\rho u_i)}{\partial x_i} = 0 \\[3mm] \dfrac{\partial(\rho u_i)}{\partial t} + \dfrac{\partial}{\partial x_j}(\rho u_i u_j + p/(\gamma Ma^2)\delta_{ij}) = \dfrac{1}{Re}\dfrac{\partial \sigma_{ij}}{\partial x_j}, \\[3mm] \dfrac{\partial E}{\partial t} + \dfrac{\partial}{\partial x_i}[(E u_i + p/(\gamma Ma^2))] = \dfrac{1}{PrRe(\gamma-1)Ma^2}\dfrac{\partial}{\partial x_i}\left(\kappa \dfrac{\partial T}{\partial x_i}\right) + \dfrac{1}{Re}\dfrac{\partial u_j \sigma_{ij}}{\partial x_i}, \end{array}\right\} \quad (2.2)$$

where $\sigma_{ij} = \mu(\partial u_i/\partial x_j + \partial u_j/\partial x_i - (2/3)(u_k/x_k)\delta_{ij})$. The above equation set is closed with the normalized equation of state: $p = \rho T$. The energy term represents the total energy, which is the sum of the internal and kinetic energies, such that $E = p/((\gamma - 1)\gamma Ma^2) + (1/2)\rho(u_i u_i)$. The normalized viscosity is uniquely a function of temperature and follows a power law of the form $\mu = T^{0.76}$.

2.2.2. *Numerical scheme*

We developed and validated a high-order predictor/corrector finite difference solver, which was used to compute the compressible Navier–Stokes equations. The spatial scheme is fourth-order accurate inside the domain with a one-sided third-order scheme at the finite boundaries. The high-order MacCormack-like scheme was chosen as the biased stencil on the convective terms provides a robust and efficient method to deal with the high gradients (without adding artificial viscosity) while offering acceptable dispersion and dissipative qualities (see Hickey (2012) for details). The greater resolution required to account for the slightly inferior numerical qualities compared to spectral or Padé schemes, for example, is offset by the computational efficiency, parallelisability and small memory footprint. The time-dependent compressible Navier–Stokes equations are solved in conservative form with skew-symmetric convective terms for robustness and reduced aliasing errors. The time was advanced using a second-order explicit scheme in which the time step was set by an imposed acoustic Courant number. The numerical code was extensively verified against the analytical solution of a viscous shock, Taylor–Green vortex and decaying compressible isotropic turbulence. Validation with experimental wake data in the incompressible limit was performed in Hickey *et al.* (2013).

2.2.3. *Grid, boundary and initials conditions*

A homogeneous grid was used in the streamwise and spanwise directions. In the cross-wake direction, the grid was clustered about the centreline using a hyperbolic tangent mapping. The grid resolution was chosen to resolve down to the Kolmogorov scale for the entire evolution of the wake. As the flow is temporally evolving, periodic boundary conditions were set in the streamwise (x) and spanwise (z) directions. In the cross-wake direction (y), non-reflecting boundary conditions (Thompson 1990), supplemented with sponge layers, were used to attenuate spurious numerical oscillations at the boundaries. The domain size was selected to be at least eight times the most unstable anti-symmetric wavelength in the streamwise direction and four times the most unstable oblique symmetric mode in the spanwise direction. Consequently, the domain sizes are Mach number dependent. In the cross-wake, the domain height was chosen large enough to accommodate at least six wake half-widths at all times during the simulation. The very large computational domain was justified by the need to enhance the sampling of higher-order statistics, to reduce the dependence of the domain size on the developing instability modes and to allow the growth of the long-wavelength, oblique varicose mode.

The simulations are temporally evolving. Although temporal simulations remain of great scientific interest, they fall short in faithfully reproducing the transition of wake flows. On the one hand, the temporal simulations require a parallel flow assumption, which is not entirely valid in the case of transitional wakes. In addition, the instability modes are unable to spatially grow, as would occur in a spatial simulation or experimental set-up, and are constrained by the computational domain. A final issue concerns the infinite propagation in the streamwise and spanwise direction of acoustical, vortical and entropic perturbations. These perturbations then recontaminate

Ma	Re	Grid size	Domain size	$\eta/\Delta x|_{min}$
0.8	3000	$1600 \times 496 \times 596$	$67.9 \times 20 \times 26.1$	0.61
2.0	3000	$1792 \times 496 \times 696$	$78.3 \times 20 \times 29.9$	0.88

TABLE 1. Characteristics of the numerical simulations of the transitional wake. The $\eta/\Delta x|_{min}$ represents the minimal value over the domain, during the entire transitional simulation.

the computational domain, whereas in the spatial case, they are simply advected out of the domain. Despite these valid concerns, the study of temporal transition of free-shear flow remains valuable in understanding transitional mechanism. Many temporal studies of high-speed free-shear flows have shown convincing quantitative matching of experimental results (e.g. Pantano & Sarkar 2002). Furthermore, the correct physical mechanisms of the temporally evolving simulations are extensively reported (Rempfer 2003). In addition, the temporal wake evolves without a receptive trailing edge and therefore we are able to isolate the intrinsic wake transition from the wake generating body. Furthermore, given the lengthy transition caused by the increasing stability of the high-speed wake, we are able to simulate higher Reynolds number flows than could be afforded by a spatial simulation.

The wakes were simulated at a constant Reynolds number of 3000, based on the initial wake half-width and initial velocity defect, at two different initial relative Mach numbers: $Ma = 0.8$ and 2.0 (herein, the wakes are identified by their initial Ma_r; for clarity, the subscript 'r' from Ma_r is dropped). To fully resolve all the scales of turbulence, a grid of 473 and 619 million nodes, respectively, was needed, see the numerical details in table 1. A laminar initial velocity profile was used: $\langle u(y) \rangle = U_\infty - U_d \exp(-\ln(2)y/b)^2$ where U_∞, U_d and b are respectively the free-stream velocity, the initial deficit velocity and the initial wake half-width. Admittedly, the choice of a Gaussian, instead of a double Blasius profile, may inhibit the development of near-wake instability modes originating from a double boundary layer profile (Papageorgiou & Smith 1989; Papageorgiou 1990). In Hickey *et al.* (2013), the evolution of a Gaussian and double Blasius wake profile were compared in the incompressible limit; other than a delayed transition, the main characteristic structures and statistics remain surprisingly similar. Based on these conclusions, we deemed that an initial Gaussian profile allows the greatest generality for the study of the temporally evolving wake. The laminar base flow velocity and temperature fields were related through the Crocco–Busemann relationship. The initial wake profile is perturbed by broadband velocity fluctuations for the components in x- and y-directions with an r.m.s. value of 1.5 % of the velocity deficit, in order to break the symmetry about the centreline. The broadband perturbations have a greater generality but result in a longer transition compared to specific mode forcing. The initial wake half-width was unity resulting in a constant mass flux defect of $\dot{m} \approx 1$. The computations were conducted at the High Performance Computing Virtual Laboratory (HPCVL) in Kingston, Ontario using 128 processors and required a wall clock time of approximately 45 days per simulation. In addition to these computations, we conducted numerous lower Reynolds number simulations at $Re = 1500$ on a fixed computational domain ($L_x, L_y, L_z = 50, 25, 12.5$) and grid (56 million grid points) for $Ma = 0.3, 0.8, 1.2$ and 2.0. These fully resolved simulations are used to validate the generality of our results at different relative Mach numbers. Grid convergence and resolution tests are presented in the Appendix.
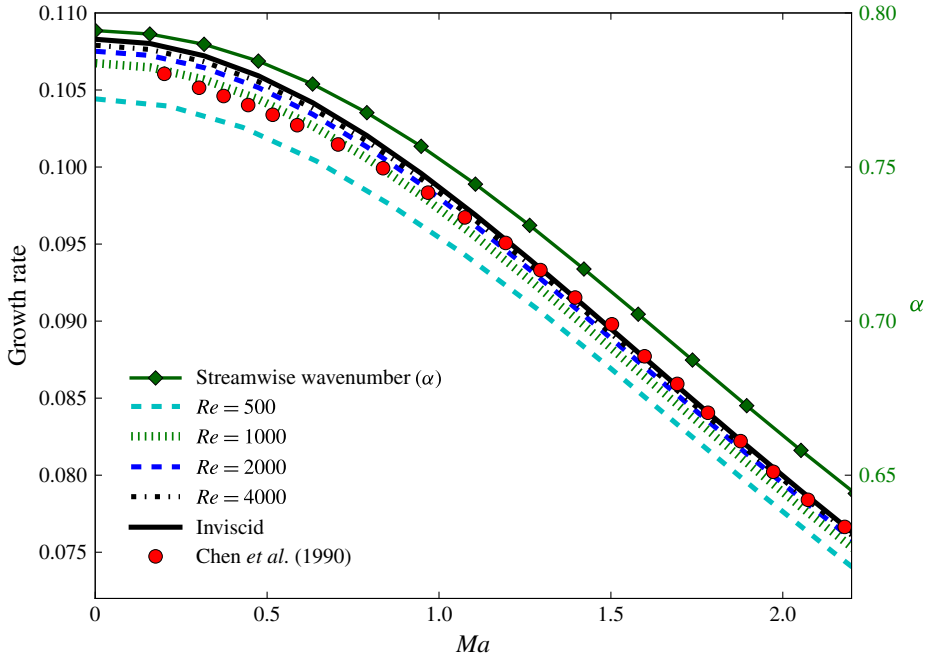
FIGURE 1. (Colour online) Influence of compressibility and viscosity on the maximal growth rate of the instability modes (two-dimensional, anti-symmetric mode). The maximal exponential growth for Reynolds numbers of 500, 1000, 2000 and 4000 are compared with the inviscid results by Chen *et al.* (1990). The streamwise wavenumber of the most unstable mode (squares) is shown on the right-hand side.

3. Linear stability of high-speed wakes

Given the symmetry of the laminar base flow, two classes of instability modes arise. The anti-symmetric (or sinuous) mode is defined at the centreline as $\hat{u} = 0$ and $d\hat{v}/dy = 0$ while the symmetric (or varicose) mode is defined as $\hat{v} = 0$ and $d\hat{u}/dy = 0$. Both modes have exponentially unstable components in the two-dimensional planar wake.

3.1. *Sinuous instability mode*

As in the incompressible wake, the highest exponential growth is achieved for a purely two-dimensional, anti-symmetric (sinuous) perturbation for all Mach numbers. This perturbation results in the formation of two rows of staggered spanwise coherent rollers, sharing many characteristics with the classical Kármán vortex street in the wake of a bluff body. From previous investigations (Chen *et al.* 1990; Watanabe & Maekawa 2004), an increasing Mach number decreases the maximal exponential growth of the primary disturbance. Between free-stream Mach numbers of $Ma = 0.01$ and 2.0, the exponential growth rate is reduced by approximately 30 %, see figure 1; a modest decrease compared with the very drastic drop in growth rates observed in the mixing layer (a reduction of approximately 18 % from the incompressible growth rate at $Ma_c = 0.4$ % and 72 % at $Ma_c = 1.2$ (Sandham & Reynolds 1990)). The viscosity has a slightly stabilizing effect on the high-speed wake. Although the stabilizing effect of viscosity is minimal compared with the inflectional instability of
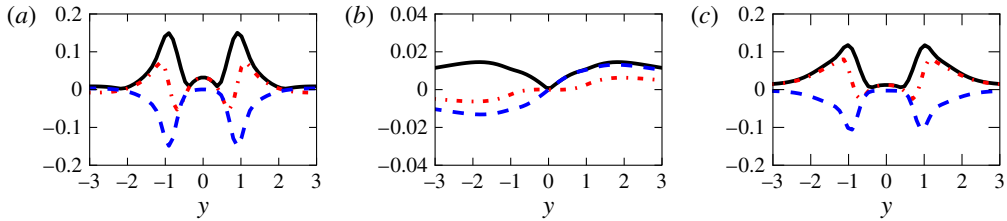
FIGURE 2. (Colour online) Eigenvectors of the most unstable mode at $Re = 10\,000$ at $Ma = 1.92$ ($\alpha = 0.239$, $\beta = 0.264$). The real (red line, dashed-dot), imaginary (blue line, dashed) and the magnitude (black line, full) are presented for $\hat{u}$ (a), $\hat{v}$ (b) and $\hat{\rho}$ (c).
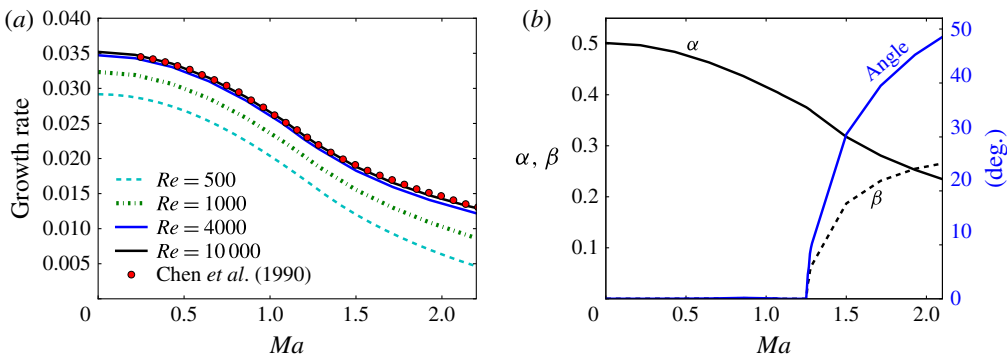

FIGURE 3. (Colour online) Influence of compressibility and viscosity on the varicose (two- and three-dimensional, symmetric perturbation) mode in the high-speed wake. The viscosity has a strong stabilizing effect on the growth (top). The streamwise and spanwise wavenumbers of the most unstable symmetric mode for $Re = 10\,000$ are presented along with the corresponding angle of the optimal disturbance.

the mean profile. As noted by Watanabe & Maekawa (2004), there is less than 2 % difference between growth rate at $Re = 1000$ and the fully inviscid case for all Mach numbers studied, see figure 1. Overshadowed in the previous studies is the striking correlation between the growth rate and the wavelength of the most unstable mode. The wavelength of the most unstable mode is similarly approximately 18 % longer at a Mach number of 2.0 compared to the incompressible baseline. The concomitant effects of an increased wavelength are discussed in the following sections and are central to our understanding of high-speed wake transition.

3.2. *Varicose instability mode*

The symmetric (varicose) mode plays a secondary role in the transitional mechanism of the high-speed wake, as growth rate is less than a third of the primary anti-symmetric instability. Nonetheless, the importance of the symmetric mode cannot be neglected as it may modulate the anti-symmetric mode, as noted in the incompressible case by Wygnanski, Champagne & Marasli (1986). For completeness, figure 2 shows the eigenvectors of the most unstable varicose mode. The influence of this mode is particularly important for high-speed wakes as it shifts from a purely two-dimensional to an oblique perturbation at approximately $Ma = 1.2$ (see figure 3) as previously observed by Chen *et al.* (1990) and Watanabe & Maekawa (2004).

This raises the question of why the symmetric mode has a drastic jump in the appearance of a cross-wise component to the instability. This observation recalls the onset of three-dimensionality in the transitional high-speed mixing layer above a convective Mach number of 0.6. To the best of the authors' knowledge the exact physical mechanism of this jump in the mixing layer remains elusive. Similar to the primary mode, the symmetric instability mode is damped by both viscous and compressibility effects. The viscous effects play an important role in impeding the growth of this mode. Figure 3 shows that at $Re = 1000$, the exponential growth rate is 10 % lower than the inviscid case at $Ma = 0.001$ – at Mach number 2.0, it is 30 % lower. The varicose mode is nearly completely suppressed for Reynolds numbers under 250. In addition to the stabilizing effect of viscosity, the wavelength of the symmetric mode is over twice that the anti-symmetric mode over all the Mach numbers investigated. The combined effects of an inhibited growth rate caused by viscosity and the longer instability wavelength may have hindered the observation of the emergence of this three-dimensional mode in the previous direct numerical simulations of transitioning high-speed wakes. Those simulations at $Re = 300$ (Chen *et al.* 1990) and 1000 (Watanabe & Maekawa 2004) were on computational domains clearly too small to capture the varicose modes. As a result, the effects of the three-dimensional symmetric mode were probably inhibited. These observations invite a new investigation, at higher Reynolds number and on a larger domain in order to accommodate the longer wavelengths.

4. Domain of influence in the transitional wake

In free-shear flows, the wavelength imposed by the fastest growing instability mode characterizes the length scale of the emerging transitional structures. Based on the results from linear stability theory § 3 (assuming no external forcing), it comes as no surprise that the rollers emerge as purely two-dimensional structures with an increasing wavelength with increasing *Ma* number. The increased wavelength of the primary instability mode leads to two, seemingly trivial, features of the high-speed wake transition: (i) increased streamwise separation between neighbouring rollers on the same row; and hence (ii) increased circulation of each roller. For a fixed wake half-width of the base flow, b, compressibility decreases the ratio of the cross-wake to streamwise separation, h/λ, where h represents the cross-wake separation between rows (which is, to a close approximation, a function of the wake half-width, b) and λ the streamwise separation between neighbouring rollers (being related the most unstable wavelength). In the present section, we consider the compressibility effects on the acoustic propagation and the domain of influence in the laminar base state of the high-speed planar wake.

4.1. *Domain of influence in the transitional compressible wake*

The staggered array of spanwise vortices, forming a Kármán vortex-like street, has been shown to be unstable to infinitesimal perturbations for two-dimensional vortex filaments in the inviscid case, except for the well-known neutrally stable configuration of $h/\lambda = 0.28055$. Using an inviscid hollow vortex model, Crowdy & Green (2011) showed a cross-over point at an aspect ratio of $h/\lambda = 0.34$–0.36. Above this threshold, pairing occurs between neighbouring rollers on the same side, as typically observed in most low-speed transitioning wakes. Below this threshold, it occurs between rollers from across the centreplane (merger between rollers with opposite circulation, clearly breaking up and then decimating both rollers due to cross-diffusion of vorticity). The stability properties of such flows were considered in Llewellyn Smith & Crowdy (2012).

Although it is tempting to infer the stability features from incompressible vortex dynamics, this approach is invalid for high-speed flows as the domain of influence of each roller is no longer global. The classic Biot–Savart induction law is not directly applicable to compressible flows, partly because of the dilatational component of the flow, but more importantly, because the induced velocity follows the characteristic lines (Smits & Dussauge 2006) which are modified by the gradient of the mean flow. To address this issue, we approximate the characteristic lines (which we assume to be the communication path) of a single point within a laminar wake profile in order to infer the domain of influence of a compact roller.

The path of communication in compressible flows follows the characteristic lines. In a high-speed free-shear flow, the mean Mach gradient modifies the path of the characteristic wavefronts. As a result, communication between two neighbouring rollers may be hindered, possibly even completely cutoff. Despite the simplicity of the approach, the geometric evaluation of the ray paths have been shown by Papamoschou (1994) to offer a good qualitative and quantitative comparison with the characteristic-based computations from the linearized equations of motion. In order to investigate the compressibility effects on the communication paths in the high-speed wake, we extend the analysis of the mixing layer (Papamoschou 1993, 1994; Papamoschou & Lele 1993) to consider the symmetric profile of the high-speed wake. Assuming a constant speed of sound, the generalized form of Snell's law relating the direction of acoustic propagation to the local *Ma* is

$$\sin \theta = \frac{\sin \theta_o}{1 + (Ma - Ma_o) \sin \theta_o}, \tag{4.1}$$

where θ is the angle from the vertical and the subscript '$_o$' represents the Mach number and angle at the origin (Ma_o, θ_o). Based on classical ray tracing theory, the trajectory can be defined as a simple ordinary differential equation in two dimensions:

$$\frac{\mathrm{d}x}{\mathrm{d}t} = U(y) - a \sin \theta; \qquad \frac{\mathrm{d}y}{\mathrm{d}t} = \pm a \cos \theta. \tag{4.2a,b}$$

Herein, we are interested in understanding the path of information propagation. For simplicity, we assume a laminar Gaussian distribution of velocity: a valid assumption even during emergence of transitional spanwise rollers. We developed a two-dimensional ray tracing tool using an explicit time advancement based on a fourth-order Runge–Kutta scheme, similar to Papamoschou (1993); the source code can be found in Hickey (2012). Figure 4 shows the path of propagation of a perturbation emitted from a source at the wake half-width (a,c,e) and at the centreplane (b,d,f). For the computations, we neglect the effect of wave dispersion or attenuation.

The path of communication is greatly influenced by the Mach number gradient of the base flow. If we approximate a single roller as a compact vortical source at the wake half-width (figure 4a,c,e), a clear increased cross-wake information is observed with increasing *Ma*; simultaneously, the streamwise communication is inhibited. An important region of near-silence develops upstream (to the left) of the source, while a region of weak acoustic intensity develops downstream of the source (to the right). The increased cross-wake influence can also be seen in the increasing inclination of the wavefronts with *Ma*. The constitutive shear layers of the wake act as a waveguide, as such, the perturbations within the wake are internally reflected, raising the possibility of the emergence of an acoustic instability modes as in the boundary
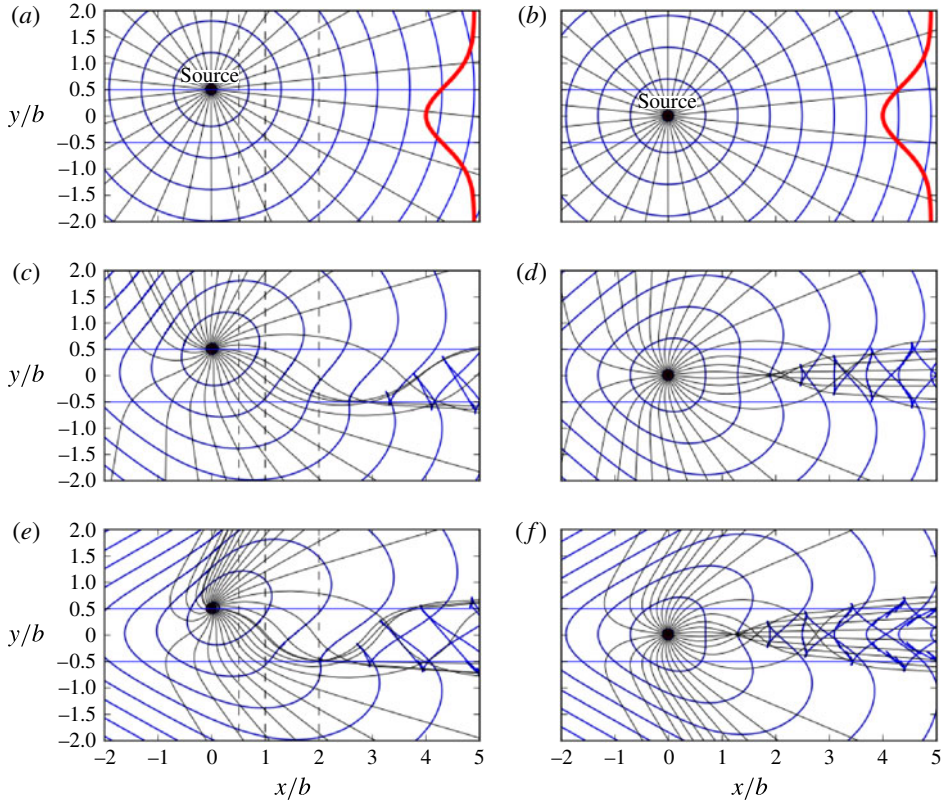
FIGURE 4. (Colour online) Propagation path of an omnidirectional acoustic disturbance in laminar wake (Gaussian profile shown in *a,b*) at $Ma_r = 0.0$, 0.5 and 1.0 (rows top to bottom) for a source at the upper inflection point of the mean velocity profile (*a,c,e*) and at the centreline (*b,d,f*). The contour lines represent the wavefronts. The dashed vertical lines represent the streamwise locations of signal intensity measurements in figure 5.

layer (Mack 1975, 1990). Interestingly, the information which does exit the waveguide is preferentially inclined to the free stream with an increasing streamwise orientation with Mach number, recalling the findings of acoustic waves in the free stream by Watanabe & Maekawa (2004) and Maekawa, Takiguchi & Watanabe (2006).

We recall that the acoustic intensity is proportional to the separation between two adjacent traces for an omnidirectional acoustic source (Papamoschou 1993): the closer two adjacent traces are to each other, the stronger the signal (valid under the assumption of zero wave dispersion or attenuation). Hayes (1968) formalized the energy conservation law for geometric acoustics in a moving medium. From figure 4 at $Ma = 0.5$ and 1.0, we can infer the important effect of compressibility on the intensity of the acoustic disturbance. A very weak acoustic signal is found between 1.5 and 3.5 wake half-widths downstream (to the right of the source), which represents the typical streamwise separation between adjacent rollers in the transitional high-speed wakes. To quantify this effect, the intensity of the acoustic signal is computed at three streamwise locations (shown as vertical dashed lines in figure 4*a,c,e*) for an acoustic source at the inflection point of the wake. The relative acoustic intensity profile is shown in figure 5. For the fully incompressible case, the
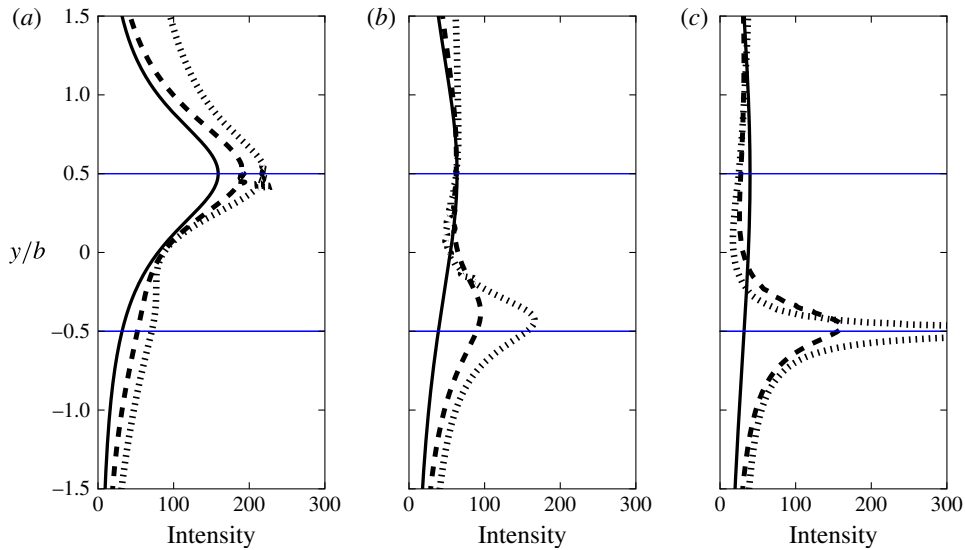
FIGURE 5. (Colour online) Relative intensity profile of an omnidirectional acoustic source at $(x/b, y/b) = (0, 0.5)$ at various streamwise locations for a free-stream Mach number of 0 (solid line), 0.5 (dashed line) and 1.0 (dotted line): (*a*) $x/b = 0.5$; (*b*) $x/b = 1.25$; (*c*) $x/b = 2.0$. The streamwise locations are identified in figure 4(*a,c,e*) by dashed vertical lines.

relative intensity of the signal is directly proportional to the distance from the source which can be seen in the Gaussian distribution of the acoustic intensity at various streamwise locations. As the free-stream Mach number increases, the relative intensity of the acoustic signal along the same row ($y/b = 0.5$) decreases with respect to the incompressible baseline. Simultaneously, the signal strength increases on the opposite side of the wake ($y/b = -0.5$).

Following the approach by Papamoschou (1993), the integrated intensity of the acoustic signal crossing the centreplane of the wake is shown in figure 6(*a*). Similar to the shear layer, the integrated acoustic intensity crossing the wake centreplane decreases monotonically with the free-stream *Ma* (for an omnidirectional source located at the wake half-width). But compressibility effects modify the distribution of the acoustic intensity along the centreplane. The acoustic intensity becomes increasingly localized with increasing compressibility of the base flow. Figure 6(*b*) shows the normalized acoustic energy distribution along the centreplane. The angle of the peak acoustic intensity varies from 90° in the incompressible case to below 50° at $Ma = 2.0$. The zone of influence of a receiver located on the centreplane of a wake is shown in figure 7. As the emerging instability modes in the wake are anti-symmetric, the increasing obliquity of the zone of influence promotes a cross-wake communication between the emerging coherent structures.

5. Numerical simulation: transitional statistics

5.1. *Defining compressibility effects*

The global compressibility effect is characterized by the relative Mach number Ma_r, which is the ratio of the centreline velocity defect to the free-stream speed of sound: $Ma_r = Ma_\infty - Ma_o = (U_\infty - U_0)/c_\infty$. Unlike the mixing layer case, the level of
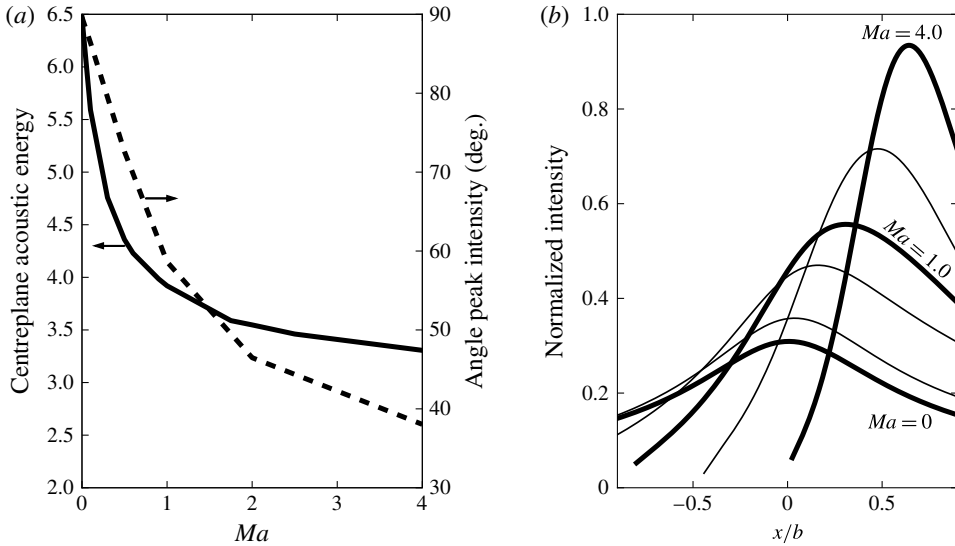
FIGURE 6. Integrated acoustic energy crossing the wake centreplane and angle with the centreplane of the peak intensity (*a*). Normalized acoustic intensity distribution along the centreplane (*b*) from an omnidirectional source located at the wake half-width.
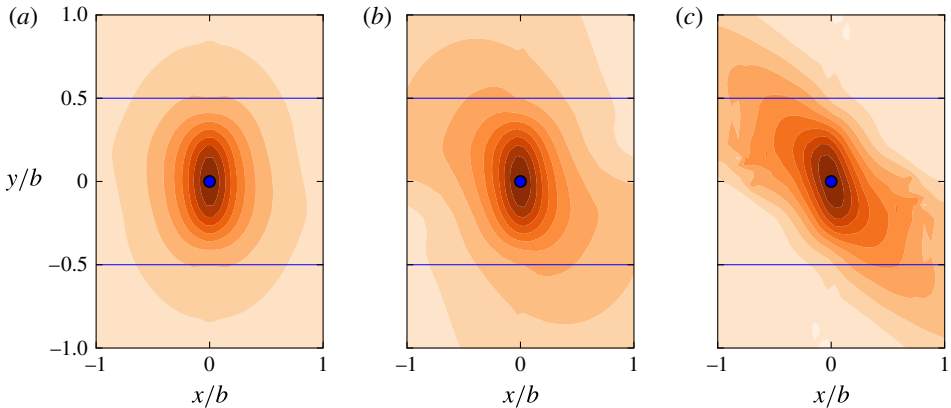

FIGURE 7. (Colour online) The Mach number effect on the zone of influence for a receiver located at (0,0): (*a*) $Ma = 0$; (*b*) $Ma = 0.5$; (*c*) $Ma = 2.0$. The isocontour lines represent the intensity of the acoustic signal at the receiver point.

compressibility in the wake decays with its evolution; the decay in time of Ma_r is shown in figure 8. Given a long enough evolution, the relative Mach number, as well as the velocity defect, asymptotically tend toward zero and the wake essentially becomes incompressible. This is not to say that the far wake of the compressible and incompressible wakes are identical. Bonnet *et al.* (1991) and Gatski & Bonnet (2009) noted clear differences in turbulence statistics in the far field between low- and high-speed wakes, the most notable difference is the peak turbulence intensity which is located further from the centreplane with increasing compressibility. Since the mean compressibility is small in the far wake, the differences are most likely
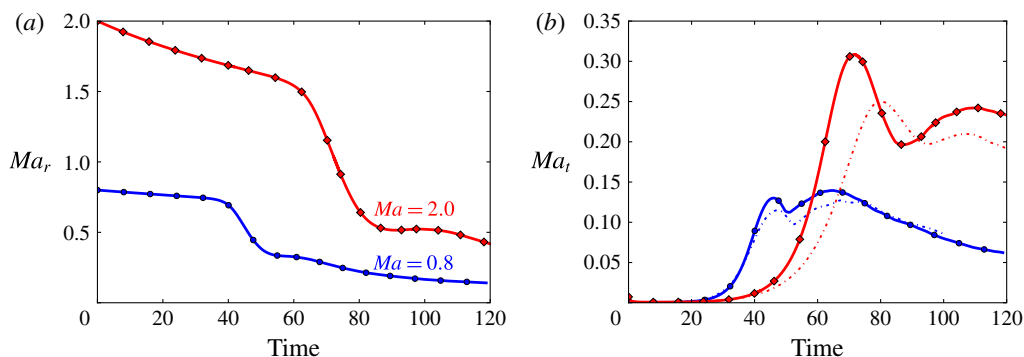
FIGURE 8. (Colour online) Evolution of the relative Mach number (*a*) and of the maximal turbulent Mach number (*b*). The dashed lines represent the $Re = 1500$ simulations.

caused by the 'memory effects' which are imparted to the flow in the near wake. A comprehensive study of the memory effects in incompressible wakes can be found in Hickey *et al.* (2013).

During the pre-transitional evolution, the centreline defect decreases faster, the lower the Reynolds number and the greater the initial Mach number. In the early nonlinear stage of transition, which roughly corresponds to the abrupt change of slope in figure 8(*a*) at the time [40–50] ($Ma = 0.8$) and [70–85] ($Ma = 2.0$), the relative Mach number decays at an increasing rate with the Mach number. The maximum slope of the relative Mach number with respect to time is -0.035 ($Ma = 0.8$) and -0.057 ($Ma = 2.0$). The trend is consistent in the lower Reynolds number simulations: -0.012 ($Ma = 0.3$), -0.028 ($Ma = 0.8$), -0.035 ($Ma = 1.2$) and -0.036 ($Ma = 2.0$), although it is unclear why the Ma should have an effect on the viscous dissipation caused by the mean flow gradient.

The turbulent Mach number characterizes the compressibility effects due to turbulent fluctuations and is defined as: $Ma_t = \langle u' \rangle_{max}/c_\infty$. The maximum turbulent Mach number is reached during transition and corresponds to: 0.1396 ($Ma = 0.8$) and 0.307 ($Ma = 2.0$). For the low-Re cases: 0.049, 0.128, 0.183 and 0.250 respectively for $Ma = 0.3$, 0.8, 1.2 and 2.0. In the far wake the turbulent Mach number monotonically decreases and follows a decay law, as in the incompressible case of $O(t^{-1/2})$. Given the initial level of compressibility of the flow, these turbulent Mach numbers are rather small, and *a priori*, should not promote the formation of any shocklets (discussed in more detail in § 5.7). To put this into context, Sandham & Reynolds (1990) did not observe any shocklets for three-dimensional mixing layers with a unitary convective Mach number. Passot & Pouquet (1987) noted that a turbulent Mach number of 0.3 was the approximate threshold for shocklet formation in decaying isotropic turbulence in two-dimensional simulations; higher turbulence Mach numbers are needed for three-dimensional simulations (Lee, Lele & Moin 1991; Samtaney, Pullin & Kosovic 2001). Note that careful checks of Ma contours failed to reveal the presence of any shocklets in the flow domain.

5.2. *Evolution of Reynolds stresses and energy budgets*

The maximal Favre-averaged turbulence statistics in the cross-wake direction (data is averaged over the periodic directions) at each time step are presented in figure 9.
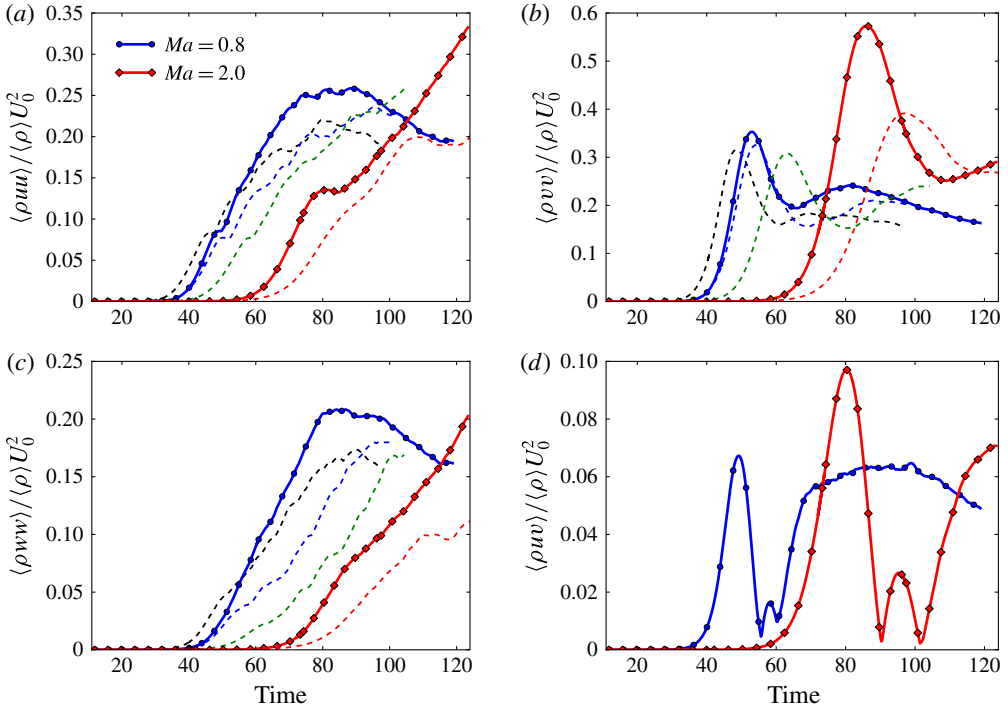
FIGURE 9. (Colour online) Evolution of the maximal Favre-averaged normalized Reynolds stresses. The dashed lines represent $Re = 1500$ cases for $Ma = 0.3$, 0.8, 1.2 and 2.0.

Other than the delayed transition, the qualitative evolution of all curves remains similar. Viscous effects are small but non-negligible when comparing $Re = 1500$ (dashed lines) and 3000 (full lines), although the relative difference between both Re increases with Ma. All wakes show a well-defined peak in vv and uv during the nonlinear stage of the transition; the peak is attributable to the roll-up process during transition. As for the incompressible cases, the peaks in the streamwise and spanwise normal stresses are rather blunt, and slowly decay to a far-field plateau which is approximately half of the peak value (Hickey *et al.* 2013). One of the principal quantitative differences in the turbulence statistics is found in the peak values reached during transition. A 53 % relative difference in the normalized cross-wake peak is observed between $Ma = 0.8$ and 2.0. Interestingly, at lower Re, the peak value is approximately constant (and shows no clear monotonic trend) for Ma between 0.3 and 1.2, while the peak at $Ma = 2.0$ is almost 19 % higher. As will be discussed in the next sections, this discrepancy between the low and high Ma peaks is related to the slightly different structural mechanisms of transition compounded with the increased anisotropy of turbulent statistics with Ma.

Figure 10 shows the normalized profiles of production, dissipation and transport at characteristic times during transition. The normalized production profiles nearly overlap, with identical peaks located at $y/b = \pm 0.45$, at both Mach numbers. A large discrepancy is found in the transport term which is very sensitive to the compressibility effects. For the higher Ma, the centreplane transport term remains a significant positive contributor to the TKE at both chosen times during transition. A
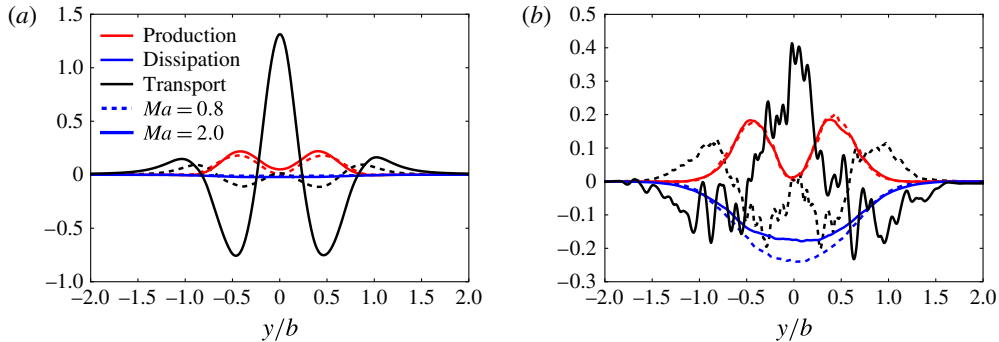
FIGURE 10. (Colour online) Normalized turbulent kinetic energy budget terms during transition at the peak $\langle vv \rangle$ ((*a*) $Ma = 0.8$ at $t = 50$; $Ma = 2.0$ at $t = 80$) and at the approximate peak $\langle uu \rangle$ ((*b*) $Ma = 0.8$ at $t = 80$; $Ma = 2.0$ at $t = 122$). The normalization parameter is U_0^3/b. Since the flow is not in an equilibrium state, the sum of the energy budget is not expected to be null. The figures provide a snapshot-averaged value of the energy budget, the lack of time averaging results in the non-smooth profile of the transport term.

discussion on the statistics of the transitional wake in the incompressible limit was undertaken in Hickey *et al.* (2013).

5.3. *Location of the maximal turbulence intensity*

The far-wake turbulence statistics by Bonnet *et al.* (1991) and Gatski & Bonnet (2009) show a clear outward shift of the location of the normalized TKE peak with increasing *Ma*. The peak shifts from approximately $y(TKE_{max})/b = 0.34$ in an incompressible far wake up to $y(TKE_{max})/b = 0.51$ at $Ma = 2.0$, where b is the wake half-width. Since the effects of compressibility are negligible in the far wake, these statistical features must be imparted to the flow in the near field (where the compressibility effects are important) and maintained through the memory effects imparted by the structures. During the early stages leading up to transition, the normalized TKE peak location remains approximately constant until transition. The cross-wake location of the normalized TKE peak increases with increasing *Ma* (see figure 11); a similarly increasing monotonic trend in the peak location is observed in lower-*Re* simulations. As rollers develop, the typical double peaks of the TKE profile is lost and the maximum turbulence intensity is located about the centreplane, as seen in figure 12; the double peak is soon regained after transition, see Hickey *et al.* (2013) for similar profiles for the incompressible wake. The centreline peak of the TKE profile during transition is the result of the induced cross-wake velocity (caused by the coherent spanwise rollers), see the time evolution of $\langle \rho vv \rangle$ in figure 9. The large cross-wake-induced velocity leads to a strong u_{rms} component along the centreplane and thus a TKE peak to shift from the outer edge of the wake to the centreline. In order to understand the structural features of transition, we investigate the location of the maximum density fluctuation, which can be considered to be an approximate surrogate for the average cross-wake location of the spanwise rollers during transition. Figure 11(*b*) shows a very distinct peak at $t = 50$ and 83 for $Ma = 0.8$ and 2.0 respectively. These peaks correspond to the exact time of the peak in $\langle \rho vv \rangle / \langle \rho \rangle U_0^2$, see figure 9. The larger the Mach number of the wake, the
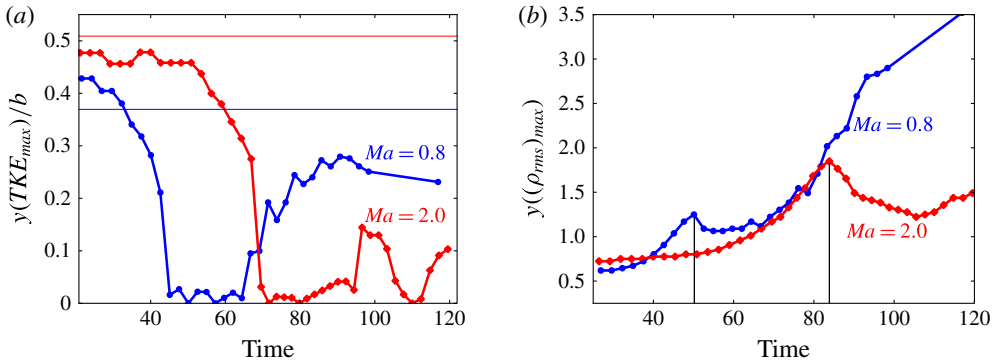
FIGURE 11. (Colour online) Evolution of the normalized cross-wake location of the maximum turbulent kinetic energy (*a*). The horizontal lines correspond to the far-wake locations of the maximum TKE for $Ma = 0.8$ and 2.0 which was interpolated from the experimental data by Bonnet *et al.* (1991, figure 3). The evolution of the location of the maximum density fluctuations (*b*).
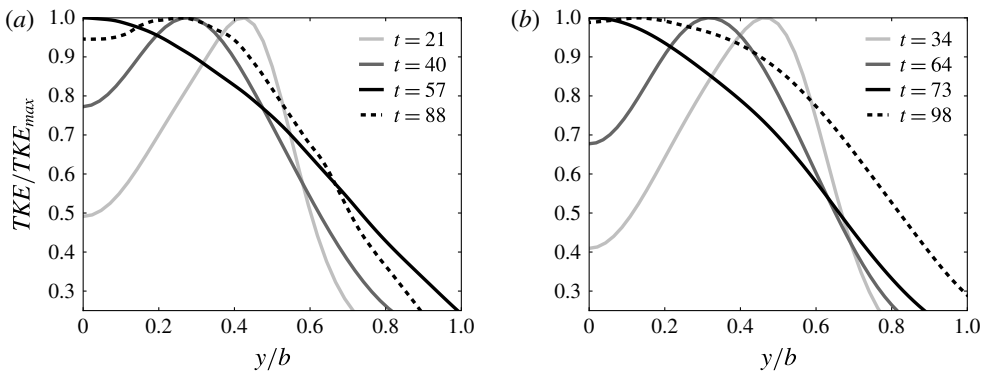

FIGURE 12. Profile of the normalized turbulent kinetic energy at three instances during the early stages of transition for $Ma = 0.8$ (*a*) and 2.0 (*b*).

farther this peak is located from the centreplane ($y_{peak} = 1.35$ ($Ma = 0.8$) and 1.85 ($Ma = 2.0$)). The structural understanding of these statistical features will be more thoroughly addressed in § 6.

5.4. *Spectral distribution of TKE*

The evolution of the spectral distribution of the TKE at the wake half-width is shown in figure 13. The peaks are visible in all the velocity components to a varying degree. The spectral peaks are found at $\kappa = 1.46$, 3.12 and 4.87 and 1.26, 2.26, 3.46 and 5.68, respectively for $Ma = 0.8$ and 2.0 (we recall that $\kappa^2 = \alpha^2 + \beta^2$). The primary wavenumbers correspond acceptably well to the theoretical results obtained from linear stability analysis (note that wavenumber of the linear stability results must be multiplied by two given the different definition of the wake half-width) which are $\kappa = 1.50$ ($Ma = 0.8$) and 1.30 ($Ma = 2.0$). Interestingly, the secondary peaks are not exact integers of the primary modes suggesting that they may be the result of secondary instability modes of the wake. Note that they do not correspond to the
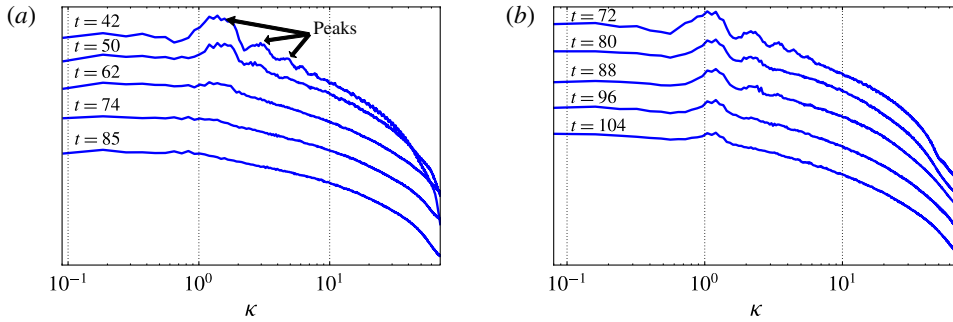
FIGURE 13. (Colour online) Spectral distribution of the turbulent kinetic energy at the wake half-width. The spectra are offset by two decades between each line: (*a*) $Ma = 0.8$; (*b*) $Ma = 2.0$.

most unstable sinuous perturbation, which has a lower wavenumber than the primary anti-symmetric instability mode. The energetic modes diffuse and the wavelength increases as the wake undergoes transition. For $Ma = 0.8$, the secondary peaks are completely lost between $t = 42$ and 50. Between $t = 50$ and 62, only the primary rollers can be identified in the spectrum and, once the wake transitions, the primary peak is completely lost. At $Ma = 2.0$, the rollers are more resilient to the scrambling of the turbulent fluctuations occurring during transition. A clear peak is observed until approximately $t = 115$, which corresponds to a very late stage of transition, recall figure 9. Although not presented, the spectral energy distribution in the spanwise direction is void of any energetic peak during transition.

5.5. *Evolution of Reynolds stress anisotropies*

The explanation for reduced turbulence production in compressible flows has often been tied to the reduction of the pressure–strain term which imposes a finite time scale (related to the acoustic propagation speed in compressible flows) to the redistribution of the TKE among the various turbulent components. As a result, the increased compressibility leads to an increased anisotropy, which we investigate during the transition of the wake. The Reynolds stress anisotropy tensor is defined as

$$b_{ij} = \frac{R_{ij} - \frac{1}{3}R_{kk}\delta_{ij}}{R_{kk}}, \tag{5.1}$$

where R_{ij} represents the ij component of the Favre-averaged Reynolds stress which is integrated in the cross-wake direction. In the high-speed mixing layer, Pantano & Sarkar (2002) showed a monotonic increase of the magnitude of the normal terms with increasing convective Mach number, but only in the near field. A similar result is observed for the transitional wake, see figure 14 and table 2. Unlike the mixing layer, the wake undergoes a return to isotropy after transition. The anisotropy in the far wake becomes negligible as the centreline defect, hence, the mean shear, tends toward zero. In the transitional region, all the peak values of the normal terms show a slight monotonic increase in magnitude with Ma, while b_{12} shows a clear decrease; a similar trend is observed among the lower-Re simulations. The most significant effect of compressibility is noted in the pre-transitional anisotropy where the difference between b_{11} and b_{22} increases, rather significantly, with the Mach number of the flow. As the pre-transitional flow is primarily two-dimensional $R_{33} \approx 0$, it is expected that b_{11} and b_{22} have a similar but opposite behaviour and that R_{11} is largest contributor
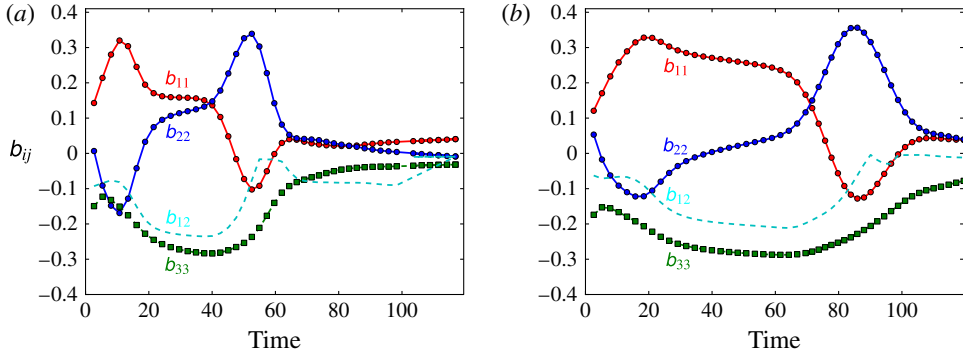
FIGURE 14. (Colour online) Evolution of the integrated Favre-averaged anisotropy for $Ma_r = 0.8$ (a) and 2.0 (b).

	Present DNS		Mixing layer		
Ma	0.8	2.0	0.3	0.7	1.1
b_{11}	0.320	0.328	0.26	0.29	0.36
b_{22}	0.339	0.356	−0.16	−0.19	−0.22
b_{33}	−0.284	−0.288	—	—	—
b_{12}	−0.235	−0.211	0.19	0.19	0.19

TABLE 2. Peak values of the Favre-averaged Reynolds stress anisotropy for the near-wake evolution. The mixing layer results are obtained from Pantano & Sarkar (2002).

to R_{kk} (since it is normal to the gradient of the mean flow). The cross-over between b_{11} and b_{22} occurs as the spanwise coherent rollers emerge in the transitional wake and contributes to important cross-wake mixing. These general results are very similar to those in the high-speed mixing layer (Pantano & Sarkar 2002). The importance of the anisotropy can be seen in the recent advances in turbulence modelling for second-order closure. Recent three-equation turbulence models (Yoshizawa *et al.* 2012) have attempted to capture the Reynolds stress anisotropy through the formation of a supersonic non-equilibrium parameters (which is a function of Ma_t), which in turn results in a reduced spread rate in the high-speed mixing layer.

5.6. *Transitional convection velocity*

The velocity of convecting structures in free-shear flows plays a central role in the entrainment of ambient fluid into the turbulent flow. In bluff-body wakes, any modification to the convective velocity is therefore tied to the base pressure (Kastengren, Dutton & Elliot 2007) and, consequently, the total drag of a body. The effects of compressibility on the convection velocity of free-shear flows have been subject to much debate, especially for the mixing layer. It has been suggested that at high convective Mach numbers, the isentropic approximation does not capture the velocity of convecting structures (Clemens & Mungal 1995): the convection velocity is either higher or lower depending on the sub or supersonic nature of the co-flowing streams. Other workers have suggested that the experimental difficulties of computing this velocity may explain the non-isotropic convection velocity results (Thurow *et al.* 2008).
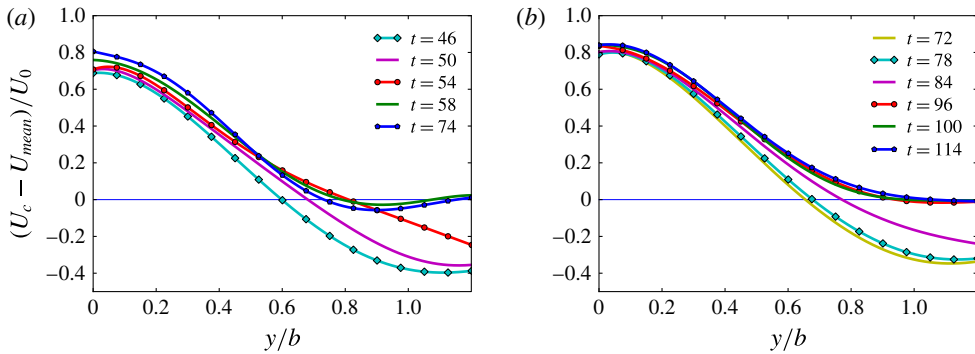
FIGURE 15. (Colour online) Convection velocity at various temporal locations during transition of the wake: (a) $Ma_r = 0.8$; (b) $Ma_r = 2.0$. A fourth-order polynomial is used to interpolate all the discrete convective velocity profiles for clarity. The convection velocity is based on the separation distance which maximizes the two-point correlation of density, ρ, with $\tau = 4$.

Any modification to the convection velocity caused by the compressibility effects in the transitioning wake would greatly modify the dynamics of the flow and this issue needs to be addressed for completeness. Different approaches to the computation of the convective velocity have been proposed. To investigate Taylor's hypothesis, del Alamo & Jimenez (2009) computed the convective velocity in spectral space, Hussain & Clark (1981) proposed a method based on the frequency–wavenumber spectrum peak while Demetriades (1976) suggested a spatio-temporal correlation approach. In the present work, the latter approach is used by finding the streamwise separation, δx, which maximizes the peak cross-correlation coefficient for a given temporal separation τ; a similar approach was also used by Kim & Hussain (1993). Therefore, the convection velocity of the structures is defined as

$$U_c = \frac{\delta x}{\tau}. \tag{5.2}$$

As the δx is confined to a finite grid, we must judiciously choose a minimal temporal separation, τ, which allows enough resolution to adequately determine the convection velocity. If τ is too small, the convection velocity becomes limited by the spatial resolution of the simulation. Alternatively, if τ is too large, the convection velocity becomes an average value of little physical interest and the inherent parallel flow assumption in this approach becomes questionable. For the current cases, $\tau = 4$ was chosen as a baseline, it should be noted that the results remain unchanged for $\tau = 8$. The density is used to identify the maximal cross-correlation coefficient, although other variables such as velocity, pressure and scalar field have also been used employing the same procedure and yielded very similar results.

Figure 15 presents the difference between the local convection and mean velocity normalized by the centreline defect. As the instantaneous convection velocity represents an averaged value over a finite time window ($\tau = 4$), the mean and centreline velocities are computed over the same temporal span. The convection velocity at the centreline differs drastically from the mean flow, the identified structures convect at significantly faster speed than the mean centreline velocity. This result should come as no surprise since any structure which drifts toward the
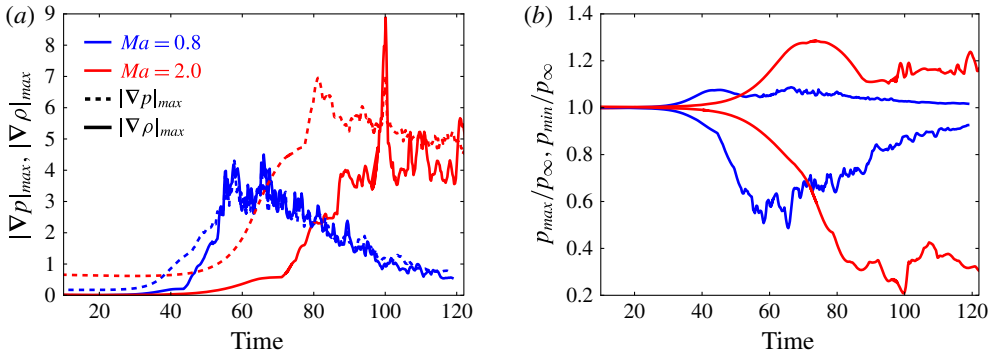
FIGURE 16. (Colour online) Evolution of the magnitude of the maximum pressure and density gradient (*a*) and the minimum and maximum pressure (*b*).

centreplane will naturally have a higher velocity. Similarly, the structures drifting outside the wake have a lower velocity than the local mean flow. After transition, the convection velocity outside the wake ($\approx y/b > 1.0$) becomes equal to the mean. Interestingly, the convection velocity is invariant to the *Ma* of the wake, a result which comes as a surprise given the large centreplane discrepancy between the magnitude of the transport term, recall figure 10.

5.7. *Shocklet formation*

Shocklets is the term used to describe a localized discontinuity caused by fluctuating fields of turbulent eddies (Lee *et al.* 1991). They are known to occur in decaying isotropic turbulence (Lee *et al.* 1991; Samtaney *et al.* 2001) and in mixing layers (Sandham & Yee 1989; Papamoschou 1995; Vreman *et al.* 1996; Freund, Lele & Moin 2000*a*,*b*). In the two-dimensional mixing layer simulations, the shocklets appear at $Ma_c = 0.7$ (Sandham & Yee 1989); for three-dimensional simulations, a higher convective Mach number is needed, approximately $Ma_c = 1.2$ (Vreman *et al.* 1996). In the case of the wake, Clemens & Smith (1998) observed eddy-induced shocklets in the near-field wake ($Ma_r > 0.9$). These observations were primarily based on the inspection of PLS images from a free-stream transitioning wake at $Ma_\infty = 3$. The presence of shocklets in the transitioning wake has the potential of greatly modifying the dynamics of the flow, as shocks promote a rapid change from kinetic to internal energy (i.e. dissipation) and also alters the eddies and turbulence via vorticity–shocklet interactions. Given the low relative and turbulent Mach numbers during the nonlinear stage of transition, it comes as no surprise that shocklets are not observed in the present transitioning wakes. Nonetheless, the evolution of the maximum local pressure, $(\partial p/\partial x_i \cdot \partial p/\partial x_i)^{1/2}$, and density, $(\partial \rho/\partial x_i \cdot \partial \rho/\partial x_i)^{1/2}$, derivatives are shown in figure 16. Despite an important peak at $t = 100$ (for $Ma = 2.0$), no clear evidence of a shocklet was observed in the instantaneous velocity field. The turbulent Mach number peaks at 0.3, which is far below the minimum value for shocklets to appear in decaying isotropic turbulence.

6. Numerical simulation: structural eduction

6.1. *Formation and shape of rollers*

Based on the flow visualization, Clemens & Mungal (1995) showed that the compressibility effects modify the shape of the rollers in the mixing layer; as the
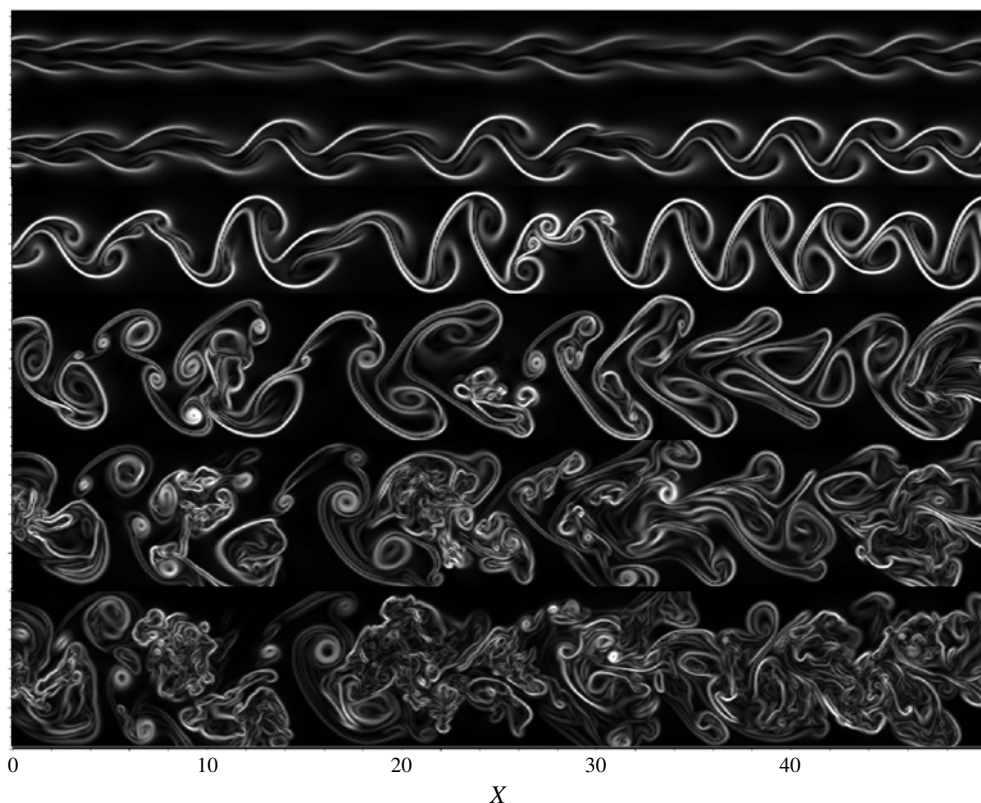
FIGURE 17. Magnitude of the density gradient (at the middle of the spanwise computational domain) for $Ma_r = 0.8$ at times (top to bottom) 41, 46, 51, 56, 62 and 76.

Ma increased, the rollers change from a circular to polygonal shape. Messersmith & Dutton (1996) showed, using a more rigorous statistical approach, that the structures become elongated and compressed with increasing compressibility. In the wake, the experimental (Clemens & Smith 1998) and numerical (Chen *et al.* 1990; Watanabe & Maekawa 2004) visualizations show initially circular rollers which deform and tend toward an elliptical shape, although from the results, it is difficult to assess if it is a transitional, a compressibility or purely shearing effect. To gain an overall understanding of the transitional structures in the planar wake, a slice of the magnitude of the density gradient, at various times, is shown in figures 17 and 18. These figures, especially figure 18, highlight some of the limitations of temporal simulations. The primary instability wavelength, as computed from the linear stability theory, dictates the streamwise extent of the computational domain. As the flow evolves and the principal wavelength becomes longer, the domain can no longer support an integer number of structures and localized cross-wake pairing may arise (see figure 18 at $t = 93$ and 109). These localized events should not limit the generality of our findings but need to be considered in the analysis.

The two-dimensional slice provides a local and instantaneous representation of the roller shape. Although the rollers are predominantly two-dimensional, there is a non-negligible variation of the shape at different spanwise locations (this will become obvious while discussing the three-dimensional structural visualizations in figures 25
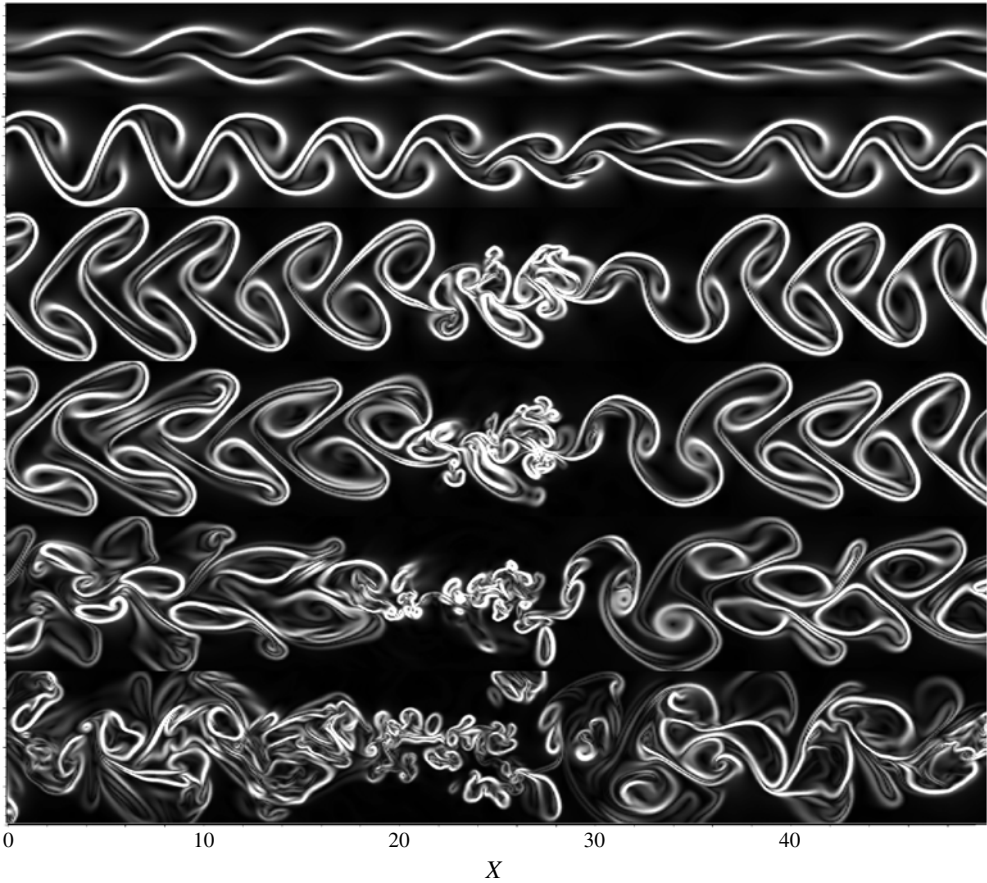
FIGURE 18. Magnitude of the density gradient (at the middle of the spanwise computational domain) for $Ma_r = 2.0$ at times (top to bottom) 66, 78, 93, 109 and 122.

and 26). These spanwise variations are attributable to the internal core dynamic instabilities of the rollers (Melander & Hussain 1994) and to local inhomogeneities (Pradeep & Hussain 2001) in the spanwise direction. Therefore, we seek to generalize the effect of compressibility on the evolution of a prototypical roller during transition. To this effect, an eduction technique based on the λ_2-criteria was developed (results are very similar when using density or Q-criteria to identify the structures).

In the first step, we agnostically average the flow in the spanwise direction and locate the mean vortex axis location by identifying the local peaks in the averaged λ_2. We visually confirm that these peaks correspond to the approximate axis of the rollers. In the second step, the rollers are extracted in the spanwise direction using a window of $b/2 \times b/2$ (in the x–y plane) around each identified peak. Each roller is remapped, using a second-order Lagrangian polynomial, onto a homogeneous grid (in the x–y plane; z is already homogeneous) with a higher resolution (71×71 for a computational domain of $b \times b$). The x–y slices at each z location are first correlated to the spanwise-averaged slice. By offsetting the slice by up to 12 grid points in each direction (which represents a maximal offset of approximately $b/6$ in x and y-directions), we identify the offset which maximizes the autocorrelation coefficient. The spanwise average, with the optimal offset, is computed with the slices which
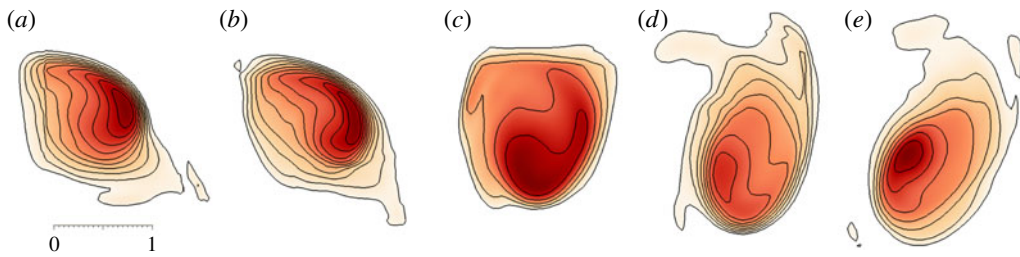
FIGURE 19. (Colour online) Evolution of the spanwise educed structure for $Ma = 0.8$ (at approximately $x = 46$) at times 46 (*a*), 48 (*b*), 52 (*c*), 54 (*d*) and 56 (*e*).
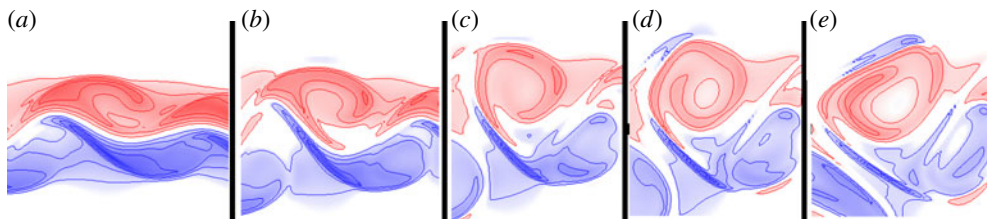

FIGURE 20. (Colour online) Formation of a roller from an instantaneous slice of the spanwise vorticity for the low Mach number case ($Ma = 0.8$). Contour lines are $\omega_z = \pm 0.25$, 0.5, 0.75 and 1.0.
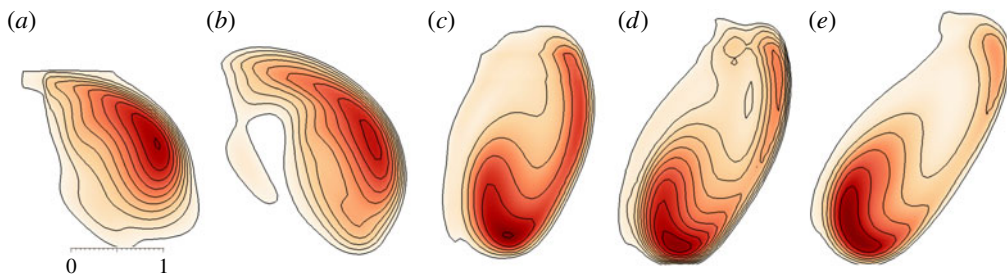

FIGURE 21. (Colour online) Evolution of the spanwise educed structure for $Ma = 2.0$ (at around $x = 42$) at times 76 (*a*), 84 (*b*), 88 (*c*), 90 (*d*) and 92 (*e*).

have an above average correlation coefficient. The remaining slices are discarded and a bootstrapping technique is used. The new spanwise-averaged roller (with optimal offset) is used to re-correlate all the slices, which are once more offset to maximize the correlation; again, only the above average correlation coefficient slices are used for the spanwise average. After 3 loops, we obtain a highly correlated coherent structure (a similar approach has been proposed by Jeong *et al.* (1997)). The evolution of the prototypical rollers during transition is unambiguously educed and presented in figures 19 and 21. In order to confirm the validity of the educed features, figures 20 and 22 show the evolution of a typical roller from a single slice of spanwise vorticity.

The effects of compressibility on the roller formation of the planar wakes is illustrated in figure 23. The increased ellipticity is a consequence of the combined effects of an increased wavelength and a reduced growth rate with increasing Mach number. Given an infinitesimal sinusoidal perturbation within a shear layer,
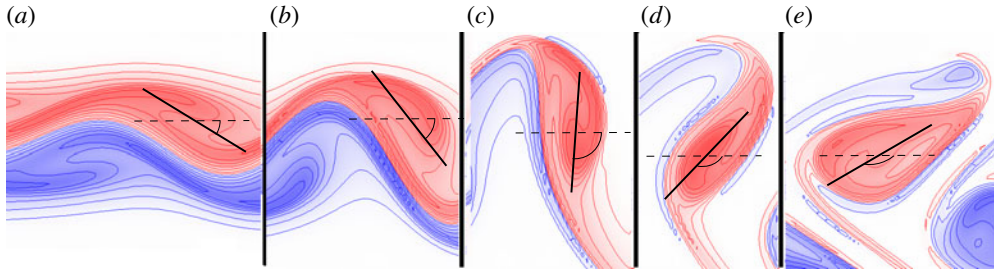
FIGURE 22. (Colour online) Formation of a roller from an instantaneous slice of the spanwise vorticity for the higher Mach number case ($Ma = 2.0$). Contour lines are $\omega_z = \pm 0.05$, 0.15, 0.3, 0.45 0.6 and 0.75. The approximate rotation angle of the principal axis of the elliptical rollers is shown: (*a*) 35°; (*b*) 50°; (*c*) 95°; (*d*) 120°; (*e*) 145°.
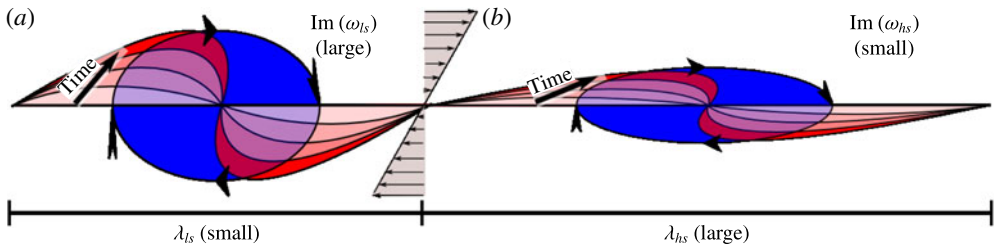

FIGURE 23. (Colour online) Conceptual sketch of the growth of a sinusoidal perturbation in a shear layer. The wavelength, λ, increases and the growth Im(ω) decreases with *Ma*. In a shear flow, the perturbations in a low-speed wake (denoted *ls*, (*a*)) will have a more circular while the high-speed wake (denoted *hs*, (*b*)) will be more elliptical. The lines correspond to the temporal evolution of a sinusoidal perturbation.

shown in figure 23, Im(ω) defines the linear grow of a perturbation in time. As the perturbation grows, the shear pushes the vorticity toward the centrepoint of the sinusoidal perturbation, hence forming the rollers. Naturally, the larger the growth rate, the faster the roll-up process. In transitional wakes, the growth rate of the most unstable mode is proportional to the conjugate diameter of the resulting elliptical structure, while the transverse diameter is characterized by the wavelength of the instability. Since the growth rate and wavelength are negatively coupled with varying Mach number (recall the linear stability theory and figure 1), it comes as no surprise that the higher Mach number (hence lower growth and longer wavelength of the most unstable mode) leads to an increased ellipticity of the transitional structures.

The increasing ellipticity with Mach number is evidenced by the educed rollers in figures 19 and 21 as well as by the two-dimensional slices of vorticity in figures 20 and 22. The present findings are in agreement with Messersmith & Dutton (1996) who suggested that compressibility elongates the coherent structures in the mixing layer. In contrast to our conceptual understanding of the roll up, the rollers show a clear asymmetry with vorticity initially congregating towards the outer-wake side of the rollers, see figures 20 and 22. As the roll-up process evolves, the point of the largest vorticity rotates at the outer radius of the roller. Interestingly, the rotation of the maximum vorticity mirrors the local peak in the location of the maximum density fluctuations (at times $t = 50$ and 83 for $Ma = 0.8$ and 2.0, respectively) in figure 11.
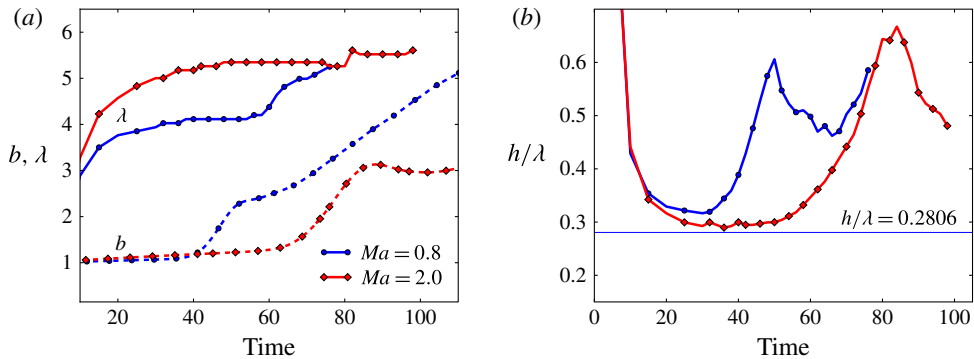
FIGURE 24. (Colour online) Evolution of the size of the spanwise rollers during transition. The separation length of the first positive peak in the two-point correlation of the cross-wake velocity was used to estimate the size of the rollers (*a*). Evolution of the ratio of the cross-wake to streamwise separation of rollers with comparative line of the neutrally stable configuration (*b*).

This result entails that the evolution of the roll-up process can be inferred from the average statistics in the wake.

6.2. *Evolution of roller configuration during transition*

The effects of compressibility on the structural configuration of the rollers is investigated. The evolution of the streamwise separation of the rollers, λ, is presented in figure 24(*a*). It is defined as the first positive peak of the two-point correlation with streamwise separation of the cross-wake velocity (λ is also invariant to the use of other velocity or thermodynamic components for the correlation) at the wake half-width. In order to unambiguously identify the first positive peak, the minimal correlation coefficient was set to -0.15 for the first negative peak and 0.1 for the first positive peak. For that reason, the values for $t > 76$ ($Ma = 0.8$) and $t > 98$ ($Ma = 2.0$) are not presented as the peaks in the streamwise correlation are too weak. As expected from the linear stability theory, the increasing Mach number results in a longer streamwise separation of the rollers. The plateau of λ during linear stage and the roller formation stage, conforms surprisingly well with the calculated wavelength of the primary instability mode from § 3.2 (recall that the wake half-width of the linear stability calculations is twice that of the DNS): $\lambda_{linear} = 4.18$ compared with $\lambda_{DNS} = 4.12$ for $Ma = 0.8$. For the higher Mach number case, the difference is slightly greater ($\lambda_{linear} = 4.83$ compared with $\lambda_{DNS} = 5.24$). It should be noted that the monoton-ically increasing wavelength with Ma is also observed for the lower-Re despite the constant computational domain size. The pairing of rollers can be seen in the increase of the streamwise separation in $Ma = 0.8$. As pairing does not occur simultaneously for all rollers, there is an incremental roller separation from $t > 60$ ($Ma = 0.8$). Interestingly, there is no noticeable increase in the length scale for $Ma = 2.0$ (and, thus, no pairing): a result corroborated by the spectral analysis in figure 13.

The evolution of the wake half-width, b, is also shown in figure 24(*a*). The initial linear stage of the wake evolution is characterized by low spread rates (up to $t = 40$ for $Ma = 0.8$ and $t = 65$ for $Ma = 2.0$). At the start of the nonlinear stage, a very rapid lateral spreading occurs during which the rollers form and rotate; recall
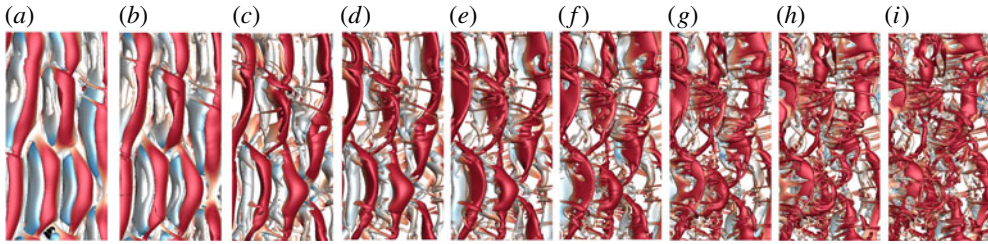
FIGURE 25. (Colour online) Top view of the transition of $Ma = 0.8$ during transition at $t = 50$ (*a*), 54 (*b*), 56 (*c*), 58 (*d*), 60 (*e*), 62 (*f*), 64 (*g*), 66 (*h*) and 68 (*i*). Isosurfaces of λ_2 coloured by the streamwise velocity. Each panel corresponds to 3/16 of the total streamwise domain ($L_x \approx 12.7$).
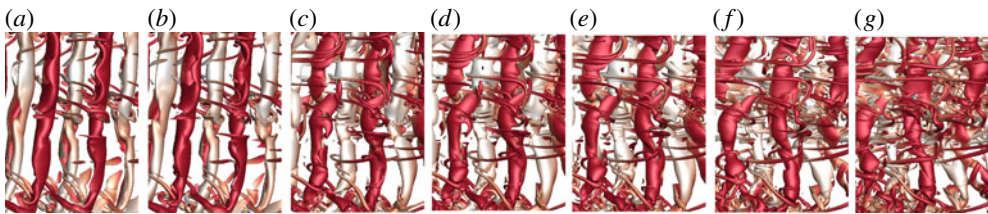

FIGURE 26. (Colour online) Top view of the transition of $Ma = 2.0$ during transition at $t = 90$ (*a*), 94 (*b*), 96 (*c*), 98 (*d*), 100 (*e*), 104 (*f*) and 108 (*g*). Isosurfaces of λ_2 coloured by the streamwise velocity. Each panel corresponds to $\approx 3/18$ of the total streamwise domain ($Lx \approx 13.1$).

figures 19 and 21. The spread rate during the roller formation stage decreases, albeit very slightly, with Mach number ($\mathrm{d}b/\mathrm{d}t = 0.1155$ and 0.1058; for $Ma = 0.8$ and 2.0, respectively). It should be noted that the lower-Re cases did not reveal a clear monotonic trend with Mach number. After the rollers form and rotate 180° (see figure 22 for the roller rotation), the lateral spreading levels off. For $Ma = 2.0$, there is even a slight, temporary decrease in the lateral length scale of the wake caused by the rotation of the elliptical rollers. As the transverse axis of the roller is oriented in the cross-wake direction (90° rotation), the wake half-width is maximized; as 180° rotation is completed and the transverse axis becomes parallel to the streamwise direction, the wake half-width is reduced, albeit temporarily.

The ratio of the cross-wake to streamwise roller separation, h/λ, (discussed in § 4) is shown in figure 24(*b*). For the cross-wake separation, we use the location of the maximum density fluctuations (figure 11) as a proxy. As expected, the ratio of h/λ decreases with increasing Mach number during the roller formation stage. As the rollers rotate, the peak density fluctuations gets pushed to the outer edge of the wake, resulting in an increasing ratio of h/λ.

6.3. *Visualization of the rollers and ribs*

The top-view visualization of the rollers, in figures 25 and 26, offers a different perspective to understand the effects of compressibility on the vortex array configuration. The cumulative effects of the increased streamwise roller separation (§ 3 and previous subsection) and an inhibited streamwise communication between rollers on the same row (§ 4) drastically modifies the interaction between the rollers.
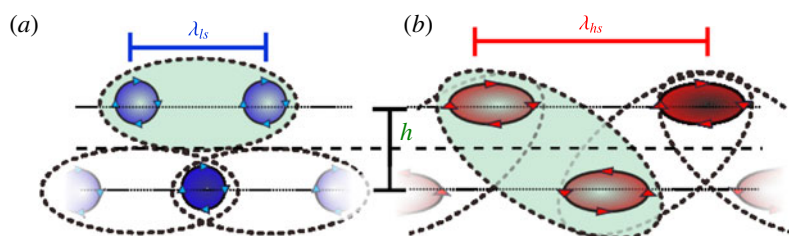
FIGURE 27. (Colour online) Illustrative effects of compressibility on the domain of influence of the rollers. In typical low-speed wakes (*ls*), communication occurs primarily between neighbouring vortices along the same row (*a*). In higher-speed wakes (*hs*), the domain of influence is predominantly in the cross-wake direction (*b*).
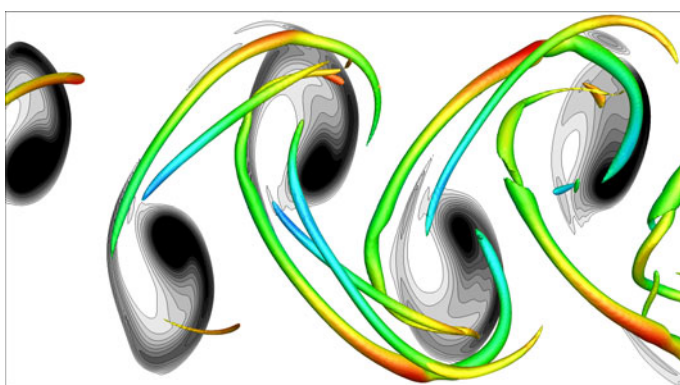

FIGURE 28. (Colour online) Organization of the rib vortices (isosurface of $Q = 0.5$) with respect to the spanwise rollers at $Ma = 2.0$ at $t = 92$. The rollers are identified by a two-dimensional contour plot of the λ_2-criteria.

As the compressibility effects become more important, there is an increasing cross-wake and reduced streamwise interaction, see illustration 27, which eventually impedes the pairing of rollers, as the roller pairing implies a mutual induction between neighbouring coherent structures. This inhibited pairing is observed in figure 26 and in the corresponding statistics of the streamwise separation figure 24(*a*). Presumably, in the fully turbulent region, pairing or amalgamation of turbulent rollers occurs but, unlike the $Ma = 0.8$ case in figure 25, it is not a transitional feature.

The increased cross-wake communication, longer roll-up time and the inhibited structural pairing in the high-speed wake promotes the formation of well-organized rib structures which connect rollers on the opposite side of the centreplane. Figure 28 shows the organization of the rib structures with respect to the primarily two-dimensional rollers in the case of $Ma = 2.0$. The rib-structures are highly organized and survive throughout transition: a clear contrast to the incompressible and low-speed wakes. The very-well-organized rib structures are a striking feature of the experimental work by Clemens & Smith (1998), shown in figure 29. The increased stability of the high-speed rollers results in the transition of the secondary rib structures before the principal rollers become fully turbulent. Signs of rib breakdown events can be inferred from experimental visualizations by Clemens & Smith (1998) and from the numerical work by Watanabe & Maekawa (2004). The breakdown of the
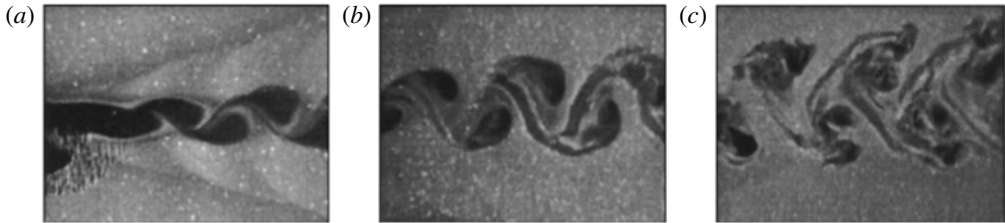
FIGURE 29. Experimental roller visualization for a planar wake at $Ma = 3.0$ (reproduced with permission from Clemens & Smith 1998).

rib structures of the high-speed planar wake was recently reported in a complementary study by Hickey & Wu (2015).

7. Discussion and conclusions

Many previous investigations have downplayed the importance of the compressibility effects in high-speed wake flows. It is true, at least qualitatively, that the increasing Ma does little to modify the general features of transition (e.g. two-dimensionality of primary instability modes, rib-structure formation), especially in comparison with the drastic changes observed in the transitioning high-speed mixing layer. In the present work, we highlight the insidious effects of compressibility on the emerging structures, along with the concomitant changes to the statistics during the transition of plane wakes. The structural modification is caused by two important features: (i) modification of the time and length scales imposed by the most unstable linear mode (recall figure 1), and (ii) alteration of the communication paths between neighbouring coherent structures (recall figure 4). These features modify the emerging rollers, their staggered spatial arrangement and their ability to merge during transition (recall figures 17 and 18). The effects of the structural changes on the transitional turbulence statistics are explored in the present work.

The cause of the structural differences in the emerging transitional rollers stems from a reduced exponential growth rate and an increased wavelength of the primary instability mode with increasing Ma_r. The most unstable spectral mode imposes a time and a length scale to the laminar base wake flow. Two direct consequences of the increased wavelength are: an increased streamwise separation between adjacent rollers; and an obviously increased circulation of the individual rollers. Based on a geometric interpretation of the characteristic lines in the wake, we show that with an increasing Ma, communication between neighbouring rollers is reduced along the same row but enhanced in cross-wake direction.

Direct numerical simulations support our claims inferred from theoretical considerations. Our work sheds light on the increasing ellipticity of the transitional structures in the high-speed free-shear flows. The ellipticity is a result of length and time scales imposed by the linear stability characteristics. As the exponential growth rate is reduced (slower roll up and reduced minor axis of the ellipse) and the wavelength increased (stretched major axis of the ellipse), the resulting structures become increasingly elliptical. The eduction technique clearly shows the rotation of the elliptical rollers during transition. As the highly elliptical rollers complete a 180° rotation and the transverse axis is parallel to the streamwise direction (see figure 18 at time $t = 93$) the wake spreading is temporally hindered as the contribution of the rollers to the mean velocity is located closer to the centreplane. For the $Ma = 2.0$ case,

there is even a temporary decrease of the wake half-width. The increased ellipticity of the rotating rollers acts to push the structures further away from the centreplane. It can be inferred that the structures, located farther from the centreplane, impart a memory to the wake which results in the outward drift of the maximum TKE location with increasing Mach number experimentally observed by Bonnet *et al.* (1991) and Gatski & Bonnet (2009). A far-wake compressible planar wake simulation would be necessary to unequivocally confirm this hypothesis.

The simulation results also revealed that the increased streamwise separation and inhibited streamwise communication eventually limit the roller pairing: an important feature of low-speed wake transition. The lack of pairing is clearly highlighted by our structural visualization between the $Ma = 0.8$ (figure 25) and 2.0 (figure 26) cases. Interestingly, the lack of roller pairing means that there is an increased two-dimensionality during transition with increasing Ma, a result which is also evident in the experimental visualizations of bluff-body wakes (see Nakagawa & Dahm (2006), figures 2 and 3). The three-dimensional varicose mode (for $Ma > 1.2$), found in the linear stability analysis, plays a negligible role in the wake transition. This is an expected result, since the growth rate of the primary, sinuous mode is approximately three times larger at all investigated Mach numbers. The reduced growth of the primary instability mode combined with the increased stability of the roller arrays (due to the lack of structural pairing) with increasing compressibility mean that the connecting ribs have a drastically longer life time and develop intricate structures which are very stable and well defined.

A closer look at the transitional statistics reveals that shocklets do not play a significant role in the transition of planar wake up to an initial relative Mach number of $Ma = 2.0$. Furthermore, the anisotropy of the Reynolds stress tensor is increased by the compressibility effects through an impeded pressure redistribution term, although the greatest variability is observed in the linear regime of the wake. As the wake transitions, there is a return to isotropy which is invariant to the initial level of compressibility in the wake. Finally, the convection velocity is independent of the initial Mach number during the entire transitional wake evolution.

The present work contributes to a better understanding of high-speed wake transition. Some questions raised will require further studies. Some of the unresolved are: (i) effect of ellipticity on the induced flow; (ii) stability of compressible staggered vortex array; and (iii) characterization of the maximal Mach number for roller pairing. Studies of these questions will contribute to a more comprehensive understanding of wake transition mechanisms and potentially open new paths for the control of these high-speed free-shear flows.

Appendix

Care was taken to resolve all scales of turbulence during transition. Figure 30(*a*) shows the evolution of the minimal ratio of the Kolmogorov length scale to the grid spacing during the entire simulation. For all simulations, the coarsest resolution is
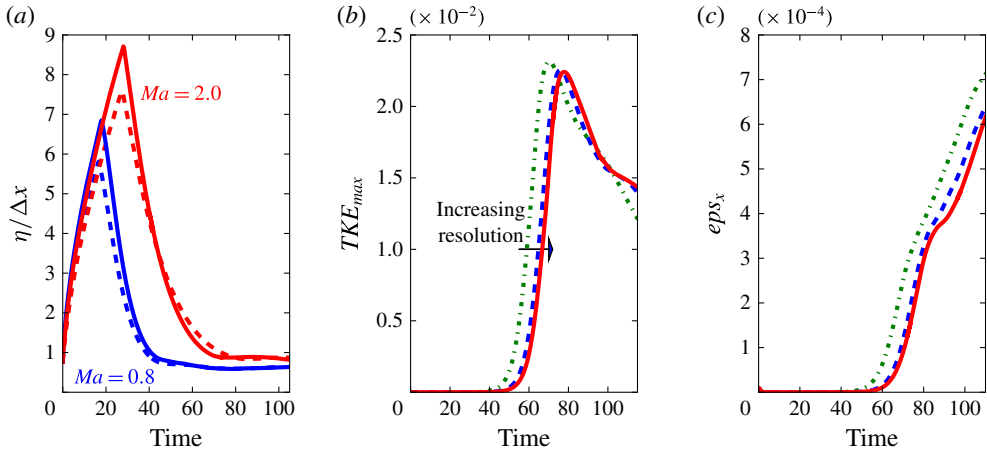
FIGURE 30. (Colour online) Evolution of the minimal ratio of $\eta/\Delta x$ during transition (*a*); simulations at $Re = 1500$ (dashed lines) and $Re = 3000$ (full lines). Grid convergence test based on the evolution of the peak turbulent kinetic energy for the wake at $Ma = 2.0$ (*b*) and the streamwise dissipation (*c*) using three different grid densities: 77, 413 and 619 million nodes.

only slightly below unity; therefore we can confidently state that all the scales of turbulence are adequately resolved by our simulations. A grid convergence study was done by comparing the evolution of the maximal turbulent kinetic energy and the streamwise dissipation for three different grid resolutions (all other parameters remained unchanged, see table 1): 77×10^6 (1/2 grid in each direction), 413×10^6 ($1/\sqrt{2}$ grid in each direction) and 619×10^6. The grid convergence is shown in figure 30(*b*,*c*); other statistical parameters such as integrated production show a similarly good agreement (less than 1.6 % of the peak production value). Needless to say that the agreement of the mean profiles are nearly perfectly captured among the different grid resolutions.

REFERENCES

DEL ALAMO, J. & JIMENEZ, J. 2009 Estimation of turbulent convection velocities and corrections to Taylor's approximations. *J. Fluid Mech.* **640**, 5–26.

ALTHAUS, W. 1990 Experimental investigation of vortex formation in the wake of a flat plate for subsonic and supersonic freestream Mach numbers. *Exp. Fluids* **9**, 267–272.

BARONE, M. F. & LELE, S. 2005 Receptivity of compressible mixing layer. *J. Fluid Mech.* **540**, 301–335.

BASTIN, F., LAFON, F. & CANDEL, S. 1997 Computation of jet mixing due to coherent structures: the plane jet case. *J. Fluid Mech.* **335**, 261–304.

BEHRENS, W. 1968 Far wake behind cylinders at hypersonic speed: II. Stability. *AIAA J.* **6** (2), 225–232.

BEHRENS, W. & KO, D. R. S. 1971 Experimental stability studies in wakes of two-dimensional slender bodies at hypersonic speeds. *AIAA J.* **9** (5), 851–857.

BLAISDELL, G. A., MANSOUR, N. N. & REYNOLDS, W. C. 1993 Compressibility effects on the growth and structure of homogeneous turbulent shear flow. *J. Fluid Mech.* **256**, 443–485.

BONNET, J.-P. & CHAPUT, E. 1986 Large-scale structures visualization in a high-Reynolds number turbulent flat plate wake at supersonic speeds. *Exp. Fluids* **4**, 350–356.

BONNET, J.-P., DELVILLE, J., SAPIN, S., SULLIVAN, P. & YERU, R. 1991 Compressibility effects in turbulent far wakes. *Eighth Symposium on Turbulent Shear Flows*.

BREIDENTHAL, R. 1992 Sonic eddy – a model for compressible turbulence. *AIAA J.* **30** (1), 101–104.

BROWN, G. L. & ROSHKO, A. 1974 On density effects and large structure in turbulent mixing layers. *J. Fluid Mech.* **64**, 775–816.

CAIN, A. B., FERZIGER, J. H. & REYNOLDS, W. C. 1984 Discrete orthogonal function expansions for non-uniform grids using the fast Fourier transform. *J. Comput. Phys.* **56**, 272–286.

CHEN, J. H., CANTWELL, B. J. & MANSOUR, N. N. 1990 The effect of Mach number on the stability of a plane supersonic wake. *Phys. Fluids* A **2**, 984–1004.

CHOI, J.-Y., MA, F. & YANG, V. 2005 Combustion oscillations in a scramjet engine combustor with transverse fuel injection. *Proc. Combust. Inst.* **30**, 2851–2858.

CLEMENS, N. & MUNGAL, M. 1995 Large-scale structure and entrainment in the supersonic mixing layer. *J. Fluid Mech.* **284**, 171–216.

CLEMENS, N. T. & SMITH, M. F. 1998 Observations of a supersonic flat plate wake transition. *AIAA J.* **36** (7), 1328–1330.

CROWDY, D. G. & GREEN, C. C. 2011 Analytical solutions for von Karman streets of hollow vortices. *Phys. Fluids* **23** (12), 126602.

DEMETRIADES, A. 1971 Observations on the transition process of two-dimensional supersonic wakes. *AIAA J.* **9** (11), 2128–2134.

DEMETRIADES, A. 1976 Turbulence correlations in a compressible wake. *J. Fluid Mech.* **74** (02), 251–267.

FOYSI, H. & SARKAR, S. 2010 The compressible mixing layer: an LES study. *Theor. Comput. Fluid Dyn.* **24**, 565–588.

FREUND, J. B., LELE, S. J. & MOIN, P. 2000a Compressibility effects in a turbulent annular mixing layer. Part 2. Mixing of a passive scalar. *J. Fluid Mech.* **421**, 269–292.

FREUND, J. B., LELE, S. J. & MOIN, P. 2000b Compressibility effects in a turbulent annular mixing layer. Part 1. Turbulence and growth rate. *J. Fluid Mech.* **421**, 229–267.

GAI, S. L., HUGHES, D. P. & PERRY, M. S. 2002 Large-scale structures and growth of a flat plate compressible wake. *AIAA J.* **40**, 1164–1169.

GATSKI, T. B. & BONNET, J. P. 2009 *Compressibility, Turbulence and High Speed Flow*. Elsevier.

HAYES, W. D. 1968 Energy invariant for geometric acoustics in a moving medium. *Phys. Fluids* **11**, 1654–1656.

HEBERT, T. 1988 Secondary instability of boundary layers. *Annu. Rev. Fluid Mech.* **20**, 487–526.

HICKEY, J.-P. 2012 Direct simulation and theoretical study of sub- and supersonic wakes. PhD thesis, Royal Military College of Canada.

HICKEY, J.-P., HUSSAIN, F. & WU, X. 2013 Role of coherent structures in multiple self-similar states of turbulent planar wakes. *J. Fluid Mech.* **731**, 312–363.

HICKEY, J.-P. & WU, X. 2015 Rib vortex breakdown in transitional high-speed planar wakes. *AIAA J.* **53** (12), 3821–3826.

HUSSAIN, A. K. M. F. & CLARK, A. R. 1981 Measurements of wavenumber-celerity spectrum in plane and axisymmetric jets. *AIAA J.* **19** (1), 51–51.

HUSSAIN, F. & DURAISAMY, K. 2011 Mechanics of viscous vortex reconnection. *Phys. Fluids* **23** (2), 021701.

JEONG, J., HUSSAIN, F., SCHOPPA, W. & KIM, J. 1997 Coherent structures near the wall in a turbulent channel flow. *J. Fluid Mech.* **332**, 185–214.

KASTENGREN, A. L., DUTTON, J. C. & ELLIOT, G. S. 2007 Large-scale structure visualization and convection velocity in supersonic blunt-base cylinder wakes. *Phys. Fluids* **19**, 015103.

KIM, J. & HUSSAIN, F. 1993 Propagation velocity of perturbations in turbulent channel flow. *Phys. Fluids* **5** (3), 695–706.

KOURTA, A. & SAUVAGE, R. 2002 Computation of supersonic mixing layers. *Phys. Fluids* **14-11**, 3790–3798.

LAUFER, J. 1975 New trends in experimental turbulence research. *Annu. Rev. Fluid Mech.* **7**, 307–326.

LEE, S., LELE, S. K. & MOIN, P. 1991 Eddy shocklets in decaying compressible turbulence. *Phys. Fluids* **3**, 658–664.

LLEWELLYN SMITH, S. G. & CROWDY, D. G. 2012 Structure and stability of hollow vortex equilibria. *J. Fluid Mech.* **691**, 178–200.

LYSENKO, V. I. 1999 Experimental studies of stability and transition in high-speed wakes. *J. Fluid Mech.* **392**, 1–26.

MACK, L. M. 1975 Linear stability theory and the problem of supersonic boundary-layer transition. *AIAA J.* **13**, 278–289.

MACK, L. M. 1990 On the insvicid acoustic-mode instability of supersonic shear flows. Part 1: two-dimensional waves. *Theor. Comput. Fluid Dyn.* **2**, 97–123.

MAEKAWA, H., TAKIGUCHI, T. & WATANABE, D. 2006 Acoustic wave generation in a compressible wake. *JSME Intl J.* B **49** (4), 1086–1091.

MELANDER, M. & HUSSAIN, F. 1994 Core dynamics on a vortex column. *Fluid Dyn. Res.* **13**, 1–37.

MESSERSMITH, N. L. & DUTTON, J. C. 1996 Characteristic features of large structures in compressible mixing layers. *AIAA J.* **34** (9), 1814–1821.

NAKAGAWA, M. & DAHM, W. J. A. 2006 Scaling properties and wave interaction in confined supersonic turbulent bluff-body wake. *AIAA J.* **44** (6), 1299–1310.

PANTANO, C. & SARKAR, S. 2002 A study of compressibility effects in the high-speed turbulent shear layer using direct simulation. *J. Fluid Mech.* **451**, 329–371.

PAPAGEORGIOU, D. T. 1990 Linear instability of the supersonic wake behind a flat plate aligned with a uniform stream. *J. Theor. Comput. Fluid Dyn.* **1** (6), 327–348.

PAPAGEORGIOU, D. T. & SMITH, F. T. 1989 Linear instability of the wake behind a flat plate placed parallel to a uniform stream. *J. Fluid Mech.* **208**, 67–89.

PAPAMOSCHOU, D. 1993 Zone of influence in the compressible shear layer. *Fluid Dyn. Res.* **11**, 217–228.

PAPAMOSCHOU, D. 1994 Characteristics of the linearized equations of motion for a compressible fluid. *Phys. Fluids* **6**, 3–5.

PAPAMOSCHOU, D. 1995 Evidence of shocklets in a counterflow supersonic shear layer. *Phys. Fluids* **7** (2), 233–235.

PAPAMOSCHOU, D. & LELE, S. 1993 Vortex-induced disturbance field in a compressible shear layer. *Phys. Fluids* **4**, 1412–1419.

PASSOT, T. & POUQUET, A. 1987 Numerical simulation of compressible homogeneous flows in the turbulent regime. *J. Fluid Mech.* **181**, 441–466.

PEREZ, R. E., JANSEN, P. W. & MARTINS, J. R. 2012 pyOpt: a Python-based object-oriented framework for nonlinear constrained optimization. *Struct. Multidiscip. Optim.* **45** (1), 101–118.

PRADEEP, D. S. & HUSSAIN, F. 2001 Core dynamics of a strained vortex: instability and transition. *J. Fluid Mech.* **447**, 247–285.

REMPFER, D. 2003 Low-dimensional modelling and numerical simulation of transition in simple shear flows. *Annu. Rev. Fluid Mech.* **35**, 229–265.

SAMTANEY, R., PULLIN, D. I. & KOSOVIC, B. 2001 Direct numerical simulation of decaying compressible turbulence and shocklet statistics. *Phys. Fluids* **13**, 1415–1430.

SANDHAM, N. 1994 The effect of compressibility on vortex pairing. *Phys. Fluids* **6** (2), 1063–1073.

SANDHAM, N. D. & REYNOLDS, W. 1990 Compressible mixing layer: linear theory and direct simulation. *AIAA J.* **28** (4), 618–624.

SANDHAM, N. D. & SANDBERG, R. D. 2009 Direct numerical simulation of the early development of a turbulent mixing layer downstream of a splitter plate. *J. Turbul.* **10** (1), 1–17.

SANDHAM, N. D. & YEE, H. C. 1989 A numerical study of a class of TVD schemes for compressible mixing layers. *Tech. Rep.* National Aeronautics and space administration.

SARKAR, S., ERLEBACHER, G. & HUSSAINI, M. Y. 1991 Direct simulation of compressible turbulence in a shear flow. *Theor. Comput. Fluid Dyn.* **2**, 291–305.

SMITS, A. J. & DUSSAUGE, J.-P. 2006 *Turbulent Shear Layers in Supersonic Flow*. Springer.

THOMPSON, K. W. 1990 Time-dependent boundary conditions for hyperbolic systems, ii. *J. Comput. Phys.* **89**, 439–461.

THUROW, B. S., JIANG, N., KIM, J. H., LEMPERT, W. & SAMIMY, M. 2008 Issues with measurements of the convective velocity of large-scale structures in the compressible shear layer of a free jet. *Phys. Fluids* **20** (6), 066101.

VIRK, D., HUSSAIN, F. & KERR, R. M. 1995 Compressible vortex reconnection. *J. Fluid Mech.* **304**, 47–86.

VREMAN, A. W., SANDHAM, N. D. & LUO, K. H. 1996 Compressible mixing layer growth rate and turbulence characteristics. *J. Fluid Mech.* **320**, 235–258.

WATANABE, D. & MAEKAWA, H. 2004 Three-dimensional evolution of structure and acoustic wave and generation in a compressible plane wake. *Fluid Dyn. Res.* **34**, 145–165.

WU, X. & HICKEY, J. P. 2012 Visualization of continuous stream of grid turbulence past the Langston turbine cascade. *AIAA J.* **50** (1), 215–224.

WU, X., JACOBS, R., HUNT, J. C. R. & DURBIN, P. A. 1999 Simulation of boundary layer transition induced by periodically passing wakes. *J. Fluid Mech.* **398**, 109–153.

WYGNANSKI, I., CHAMPAGNE, F. & MARASLI, B. 1986 On the large-scale structures in two-dimensional, small-deficit, turbulent wakes. *J. Fluid Mech.* **168**, 31–71.

YOSHIZAWA, A., ABE, H., MATSUO, Y., FUJIWARA, H. & MIZOBUCHI, Y. 2012 A Reynolds-averaged turbulence modeling approach using three transport equations for the turbulent viscosity, kinetic energy, and dissipation rate. *Phys. Fluids* **24**, 075109.

ZEMAN, O. 1990 Dilatation dissipation: the concept and application in modeling compressible mixing layers. *Phys. Fluids* A **2**, 178–188.